nature catalysis

Article

https://doi.org/10.1038/s41929-025-01368-9

Unveiling the reconstruction of copper bimetallic catalysts during CO₂ electroreduction

Received: 10 October 2023

Accepted: 4 June 2025

Published online: 14 July 2025

Check for updates

Intae Kim^{1,13}, Gi-Baek Lee^{1,13}, Sungin Kim [©] ^{2,3,12,13}, Hyun Dong Jung [©] ^{4,13}, Ji-Yong Kim [©] ¹, Taemin Lee [©] ⁵, Hyesung Choi^{2,3}, Jaeyeon Jo [©] ¹, Geosan Kang ¹, Sang-Ho Oh ¹, Woosuck Kwon ⁵, Deokgi Hong ¹, Hyoung Gyun Kim ¹, Yujin Lee ⁶, Unggi Kim ¹, Hyeontae Kim [©] ¹, Miyoung Kim [©] ¹, Seoin Back [©] ^{7,8} ∠, Jungwon Park [©] ^{2,3,9,10} ∠, Young-Chang Joo [©] ^{1,11} ∠ & Dae-Hyun Nam [©] ^{5,6} ∠

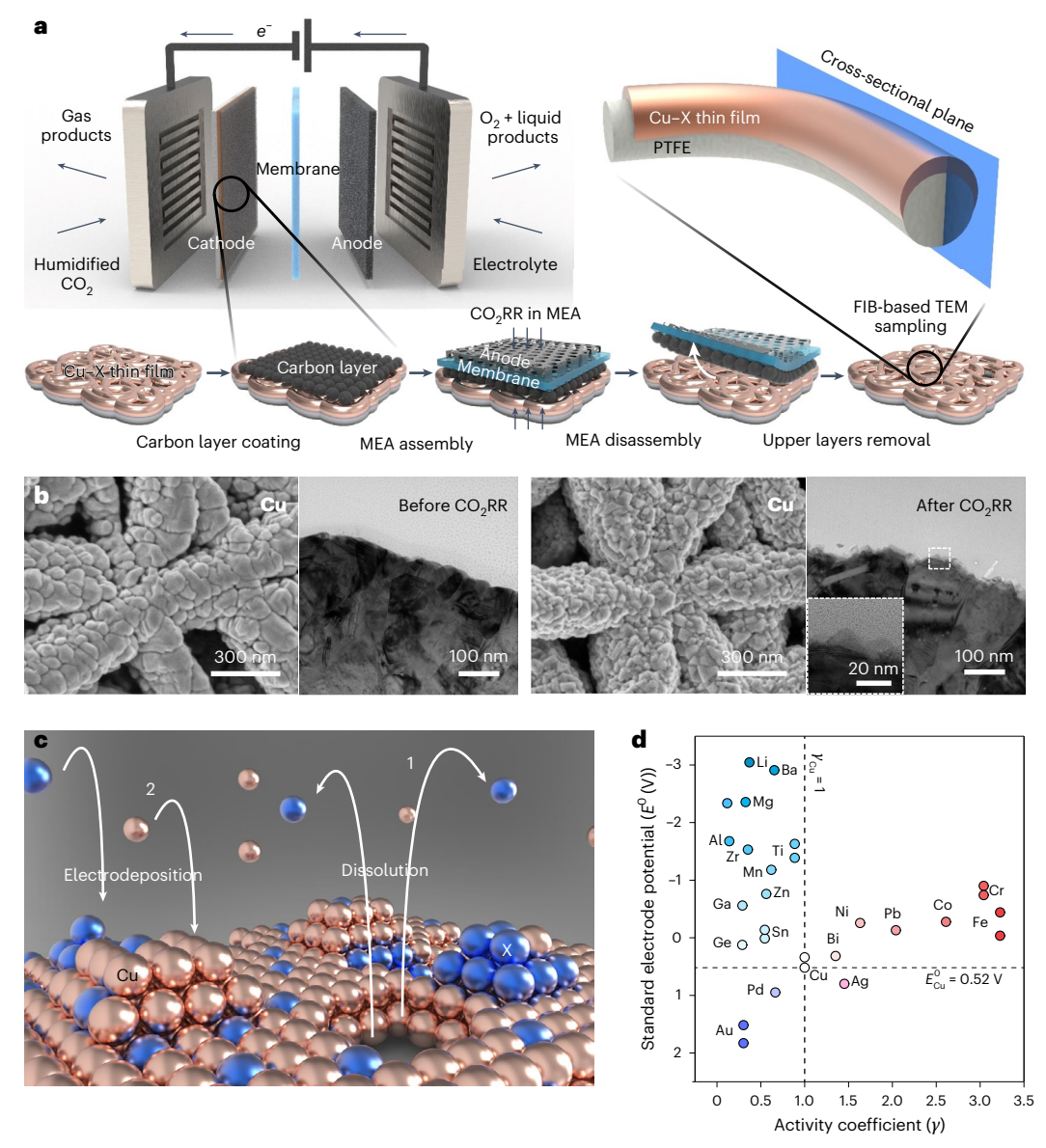
Efficient electrocatalysts should provide optimal binding sites for intermediates under operating conditions. Atomic rearrangements in catalysts during electrochemical CO₂ reduction reaction (CO₂RR) alter the original structures of active sites. Here we report a general principle for understanding and predicting the reconstruction of Cu bimetallic catalysts during CO₂RR in terms of selective dissolution–redeposition. We categorize the reconstruction trends of Cu bound to a secondary metal (X, where X = Ag, Fe, Zn or Pd) according to the oxophilicity and miscibility of Cu and X. Cross-sectional microscopy analysis of gas diffusion electrodes reveals that the surface states of reconstructed Cu-X are determined by atomic miscibility. We find that CO₂RR intermediates alter elemental preferences for dissolution, shifting them away from oxophilicity-governed behaviour and leading to selective Cu dissolution-redeposition in Cu-X. This reconstruction affects spillover in CO₂RR, controlling the selectivities of ethylene/ethanol and C₁/C₂ products. We also develop a methodology for the control of reconstruction dynamics. Our findings provide insights into designing catalysts that undergo reconstruction during electrolysis.

Electrochemical CO_2 reduction reaction ($\mathrm{CO}_2\mathrm{RR}$) has received extensive attention for its long-term energy storage and net-zero carbon emission^{1,2}. This involves multiple electron transfer and proton-coupled electron transfer steps, which result in the production of various chemicals. In $\mathrm{CO}_2\mathrm{RR}$, Cu is a representative active material that facilitates $\mathrm{C-C}$ coupling towards C_{2+} chemical production. However, steering the $\mathrm{CO}_2\mathrm{RR}$ pathway towards a specific product is challenging due to the scaling relationship of intermediate binding energies³. Introducing secondary metals into Cu can generate diverse active sites to control intermediate binding beyond the scaling relationship^{3,4}. To attempt to steer the $\mathrm{CO}_2\mathrm{RR}$ pathway, the d-band centre of active materials has been tuned through composition and interface control

in heterogeneous alloy catalysts⁵⁻⁷. However, judiciously controlled active materials undergo severe surface reconstruction, including compositional change and interface rearrangement, during $\rm CO_2RR^{8-15}$. These processes change the well-defined initial active sites and limit $\it d$ -band centre tuning.

Understanding the reconstruction of multi-metallic active materials is essential in rational catalyst design for efficient $\mathrm{CO}_2\mathrm{RR}$. Previous studies have reported on how $\mathrm{CO}_2\mathrm{RR}$ intermediates or an applied potential affect the morphology $^{16-18}$, facets 19 and chemical state 19,20 of mono-metallic catalysts by reconstruction. The reconstruction of mono-metallic catalysts has been proposed to occur by dissolution–redeposition $^{21-23}$, surface migration 16 and coalescence 24,25 .

A full list of affiliations appears at the end of the paper. e-mail: sback@korea.ac.kr; jungwonpark@snu.ac.kr; ycjoo@snu.ac.kr; dnam@korea.ac.kr



 $\label{linear_construction} \textbf{Fig. 1} | \textbf{Strategies for uncovering Cu bimetallic catalyst reconstruction in MEA-based CO_2RR. a, Schematic of the sample preparation process for investigating the surface reconstruction of Cu–X in a PTFE-based GDE after MEA-based CO_2RR. A portion of the GDE fibre was cross-sectioned using FIB to analyse the surface structure before and after CO_2RR. b, Top-view SEM images and cross-sectional-view TEM images of Cu/PTFE before and after 1 h of CO_2RR at a full cell potential$

of -3.6 V, using 0.1 M KHCO $_3$ as the anolyte in an MEA. $\mathbf c$, Schematic of the proposed stepwise processes in Cu bimetallic reconstruction. The brown and blue spheres represent Cu and X, respectively. $\mathbf d$, Thermodynamic elemental map based on the oxophilicity and miscibility of Cu and X, to classify trends in Cu–X reconstruction.

For multi-metallic catalysts, the chemical complexity of a multi-elemental system makes it more challenging to elucidate the reconstruction mechanism. Previous studies have focused on phenomenological investigations on the reconstruction behaviour of individual Cu bimetallic catalysts, such as Cu–Ag (Ag is immiscible with Cu) and Cu–Ga (Ga has a higher oxophilicity and a lower electronegativity than Cu) Moreover, CO RR in electrolysers, such as flow cells and membrane electrode assemblies (MEAs), is generally performed using gas diffusion electrodes (GDEs) for efficient CO mass transport. In the GDE, it is difficult to track the change in cross-sectional atomic distribution from the catalyst surface to the core due to the fibre-shaped gas diffusion layer, where catalysts are placed. These are the major factors that impede a fundamental understanding of multi-metallic catalyst reconstruction induced by CO RR in GDE-based electrolysers.

Here we report on a fundamental principle to assist understanding and prediction of the reconstruction of Cu-based bimetallic catalysts

during CO₂RR in GDE-based electrolysers. Using thermochemical computation, we made a thermodynamic elemental map with the descriptors of oxophilicity and atomic miscibility between Cu and various secondary metals (X) to systematically understand the reconstruction behaviours. After categorizing Cu-X into four sections, Ag, Fe, Zn and Pd were elected as X elements. Cu-X thin films were then fabricated on polytetrafluoroethylene (PTFE) fibre-based gas diffusion layers (Cu-X/ PTFE) to investigate the reconstruction behaviour under high-rate CO₂RR conditions in a zero-gap MEA, where electrodes were directly pressed against both the anion exchange membrane (AEM) and anode to minimize Ohmic loss²⁶. To preserve the surface states of active materials during MEA disassembly after CO₂RR, a sacrificial carbon layer was introduced on top of the Cu-X/PTFE electrodes. Cross-sectional transmission electron microscopy (TEM) with focused ion beam (FIB) milling enabled the investigation of lattice structures and elemental distributions of the catalyst surface while maintaining its original

morphology. Comparison of cross-sectional TEM results before and after CO₂RR revealed that reconstructed surface states strongly depend on the atomic miscibility of X with Cu. To elucidate the underlying mechanisms, in situ TEM, model studies with segmented electrodes, and theoretical calculations were conducted. These studies revealed that reconstruction is primarily driven by dynamic dissolution-redeposition during CO₂RR, with reaction intermediates promoting preferential Cu dissolution-redeposition in Cu-X, independent of oxophilicity. Furthermore, the rearrangement of Cu adatoms during redeposition is governed by atomic miscibility: Cu-X with a miscible X (where X = Znor Pd) recovers a homogeneous surface through adatom redistribution, whereas Cu-rich nanocrystals grow on Cu-X with an immiscible X (X = Ag or Fe). Reconstruction-induced rearrangement of active sites influences intermediate spillover in CO₂RR, tuning the selectivity between C_1/C_2 products and ethylene (C_2H_4) /ethanol (C_2H_5OH) . Finally, we developed a methodology to modulate reconstruction dynamics via pulsed potential cycling. For Cu-Ag, potential pulsing induced Ag intermixing into Cu adparticles, disrupting *CO dimerization sites and increasing selectivity for CO and CH₄. For Cu-Zn, pulsing-induced defective sites were preserved under CO₂RR conditions, leading to a transition of the major products from CO to C_2H_4 and C_2H_5OH .

Results

Thermodynamic strategies for investigating Cu–X reconstruction

Before investigating the reconstruction of bimetallic catalysts, we examined the reconstruction behaviour of a mono-metallic Cu catalyst induced by $\mathrm{CO}_2\mathrm{RR}$ in an MEA. Cu thin films were fabricated on porous PTFE substrates as GDEs using physical vapour deposition. A carbon black layer was then spray coated on top of the GDE to prevent direct physical contact between the catalyst layer and AEM. This sacrificial carbon (C) layer prevents the delamination of active materials from the GDE during MEA disassembly after $\mathrm{CO}_2\mathrm{RR}$ (Fig. 1a). After $\mathrm{CO}_2\mathrm{RR}$ and MEA disassembly, only the C layer/AEM/anode layers were peeled off, whereas the catalyst layer in the cathode was well preserved on the PTFE substrate (Supplementary Fig. 1). For cross-sectional analysis from the catalyst surface, we performed FIB milling on the GDE in TEM sample preparation (Supplementary Fig. 2).

Top-view scanning electron microscopy (SEM) and cross-sectional TEM analysis revealed that the original flat surface of the Cu catalyst dramatically transformed into a rough surface with numerous adparticles after 1 h of CO₂RR (Fig. 1b). In general, dissolution–redeposition has been considered the primary mechanism for surface reconstruction of CO₂RR catalysts in electrolyser configurations that include catholyte, such as H cells or flow cells 15,21,22. It was necessary to confirm whether the conditions that enable dissolution are also present in a catholyte-free MEA configuration. An isotope experiment with deuterium (D)-labelled anolyte, X-ray photoelectron spectroscopy (XPS) analysis of the cathode and inductively coupled plasma mass spectrometry (ICP-MS) analysis of the anolyte revealed anolyte crossover in the MEA, which contributed to the formation of a water layer as a dissolution medium on the cathode (Supplementary Figs. 3 and 4 and Supplementary Note 1)²⁷. The redeposition of dissolved Cu ions was also examined by tracking the formation of Cu nanoparticles on the surface of bare C-coated PTFE (Supplementary Fig. 5a). A GDE was patterned, comprising Cu/C/PTFE and C/PTFE regions (Supplementary Fig. 5b). After CO₂RR in the MEA, SEM energy-dispersive spectroscopy (EDS) analysis showed redeposited Cu nanoparticles on the C/PTFE region (Supplementary Fig. 5c). This suggests that dissolved Cu species from the Cu/C/PTFE region can migrate through the water layer and subsequently redeposit under a reductive potential.

Based on these results, we hypothesized that the reconstruction of Cu–X active materials can occur through dynamic dissolution and electrodeposition processes in a catholyte-free MEA (Fig. 1c). When Cu–X catalysts contact the electrolyte, Cu and X can be dissolved

into the electrolyte as metal ions. Redeposition of Cu and X under reductive potential during ${\rm CO_2RR}$ can create various local chemical environments.

We reasoned that the reconstruction behaviours of any Cu–X catalysts can be categorized according to the oxophilicity of X relative to Cu and the miscibility of X in Cu. We predicted that the elements with higher oxophilicity would be more vulnerable to dissolution into the electrolyte as metal ions. This redox tendency in aqueous solution is represented by the standard electrode potential (E^0). Elements with a more negative E^0 than that of Cu (E^0 = 0.34 V for Cu²⁺/Cu and E^0 = 0.52 V for Cu⁺/Cu) have a higher tendency to be dissolved out and are less likely to be electrodeposited in the Cu–X system.

While using E^0 to understand the preferential dissolution–electrodeposition in Cu–X, we utilized the activity coefficient (ν) to quantify the atomic miscibility of Cu-X and understand the arrangement of adatoms. We expected that the atomic miscibility between Cu and X can influence the interface of Cu-X after redeposition under a reductive potential. For example, when metal A and metal B are miscible, the mixing Gibbs free-energy (ΔG_{mix}) profile forms a convex curve due to the negative difference between the A-B bonding energy and the mean of the A-A and B-B bonding energies (Supplementary Fig. 6a). This indicates that A and B are preferentially intermixed to increase the number of A-B bonds, thereby lowering ΔG_{mix} . In contrast, interdiffusion is suppressed between immiscible metals, as indicated by the concave curve of ΔG_{mix} (Supplementary Fig. 6b). Here, y represents the miscibility of secondary metals in the host metal. When y is <1, the secondary metal is miscible in the host metal, allowing spontaneous interdiffusion between the two metals. Otherwise, interdiffusion is thermodynamically unfavourable due to atomic immiscibility. We calculated the activities of various metals (X) bound to Cu using a thermochemical simulation program (FactSage). The activity profiles displayed negative deviations from the ideal solution for metals miscible with Cu and positive deviations for immiscible metals (Supplementary Figs. 7 and 8).

We constructed the E^0 - γ thermodynamic elemental map to categorize the reconstructions of Cu–X active materials. On the map, Ag ($E_{\rm Ag}^0=0.80$ V; $\gamma_{\rm Ag}=1.45$), Fe ($E_{\rm Fe}^0=-0.44$ V; $\gamma_{\rm Fe}=3.23$), Zn ($E_{\rm Zn}^0=-0.76$ V; $\gamma_{\rm Zn}=0.56$) and Pd ($E_{\rm Pd}^0=0.95$ V; $\gamma_{\rm Pd}=0.67$) were selected as representative X elements by considering their oxophilicity, miscibility with Cu and tandem effect for tuning CO $_2$ RR selectivity (Fig. 1d) 28 . To control the stoichiometry of the Cu–X thin film, we employed the chip-on-target method in sputtering and adjusted the number of X chips on the Cu target (Supplementary Figs. 9–11).

Surface evolution of Cu-X active materials by CO₂RR

To investigate the structural evolution of Cu-X catalysts, we conducted top-view SEM and cross-sectional TEM and compared them before and after CO₂RR. The CO₂RR to generate the catalyst reconstruction was performed in the MEA at -3.6 V of full cell potential for 1 h. The crystal structure and elemental distribution of the catalyst surface were investigated by cross-sectional high-resolution TEM, TEM fast Fourier transform (FFT) and EDS. Before CO₂RR, Cu-X (~20 at.% X) catalysts commonly showed granular and flat surface morphology in SEM and TEM images (Fig. 2a-d). XPS analysis confirmed the clear presence and predominant metallic state of Cu and X on each Cu-X catalyst surface (Supplementary Figs. 12 and 13). In addition, X-ray diffraction (XRD) patterns, refined using the Le Bail method, were exclusively assigned to metallic Cu (Supplementary Fig. 14a-e). The FFT patterns of the Cu-X surface grains also corresponded to those of metallic Cu (Fig. 2a-d). These results indicated that secondary metals, whether miscible or immiscible with Cu, were well incorporated into the metallic Cu lattice in the as-fabricated state.

After CO_2RR , distinct differences in surface morphology were observed between immiscible (Cu–Ag and Cu–Fe) and miscible (Cu–Zn and Cu–Pd) metallic combinations (Fig. 2e–h). In Cu–Ag, crystalline adparticles with diameters of 31.3 \pm 9.4 nm formed on the surfaces of

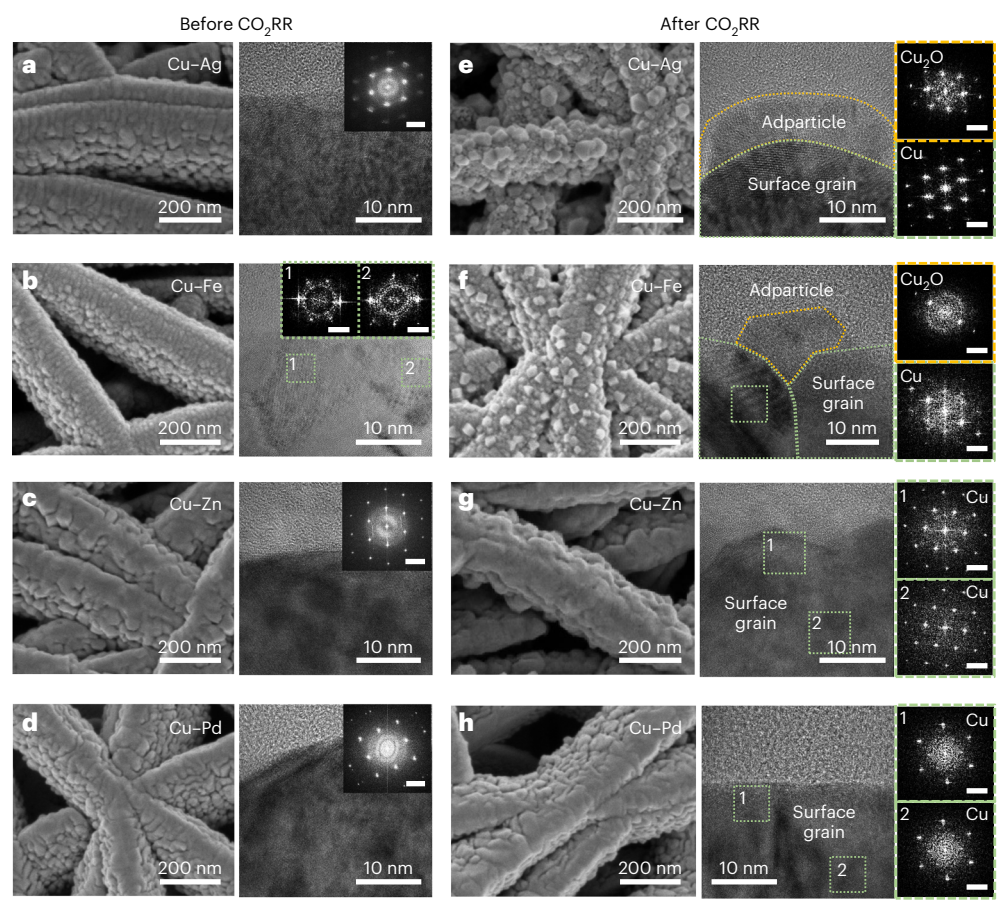


Fig. 2 | Surface structural evolution of Cu–X catalysts by CO₂RR. a–h, Top-view SEM images (left), cross-sectional-view high-resolution TEM images (right) and FFT patterns (inset) of Cu–X/PTFE GDEs (X = Ag (\mathbf{a} and \mathbf{e}), Fe (\mathbf{b} and \mathbf{f}), Zn (\mathbf{c} and \mathbf{g}) and Pd (\mathbf{d} and \mathbf{h}); -20 at.% X) before (\mathbf{a} – \mathbf{d}) an after (\mathbf{e} – \mathbf{h}) 1 h of CO₂RR at a full cell potential of –3.6 V using 0.1 M KHCO₃ as the anolyte in an MEA. In \mathbf{e} and \mathbf{f} , FFT

patterns of the adparticle (dashed orange outline) and underlying surface grain (dashed green outline) are displayed. In ${\bf b}$, ${\bf g}$ and ${\bf h}$, FFT patterns of two different positions within the surface grain (dashed green outlines) are exhibited. Scale bars in FFT patterns, $5\,{\rm nm}^{-1}$.

the catalysts after CO_2RR (Fig. 2e and Supplementary Fig. 15b). TEM FFT confirmed that the phase of the adparticle was Cu_2O , whereas the phase of the underlying surface grain was Cu (Fig. 2e and Supplementary Fig. 15d). This revealed that the roughening of the Cu-Ag surface after CO_2RR is attributed not to shape transformation but to the growth of new nanocrystals on the surface of the original catalysts. The adparticles were probably oxidized after the reductive potential was turned off, due to the nanoscale size effect 21,29 . Likewise, numerous nanosized Cu_2O adparticles were deposited on the Cu-Fe surface after CO_2RR , although the size and morphology of the adparticles were different from those of Cu-Ag (Fig. 2f and Supplementary Fig. 16). Additionally, FFT patterns in the region of the adparticles and the corresponding inverse FFT images suggested the presence of lattice defects in the adparticles evolved from Cu-Ag and Cu-Fe (Supplementary Fig. 18).

In contrast, for Cu–Zn, the original flat surfaces of the catalysts were maintained during CO_2RR . No adparticles were observed in the SEM and cross-sectional TEM images after CO_2RR (Fig. 2g and Supplementary Fig. 19b). Additionally, whole parts of the catalyst surface grains exhibited the same crystalline structure of Cu in TEM FFT analysis (Fig. 2g and Supplementary Fig. 19d). This confirmed that no new nanocrystals evolved on the surface of the original catalyst in Cu–Zn. Likewise, Cu–Pd maintained its initial smooth surface morphology and adparticles were not grown (Fig. 2h and Supplementary Fig. 20). A comparison of electrochemical surface areas before and after CO_2RR also indicated that surface roughening was suppressed in miscible combinations compared with immiscible

ones (Supplementary Figs. 21 and 22). To examine atomic-scale rearrangements beyond morphological change, we carried out atomic-resolution scanning transmission electron microscopy (STEM) imaging on cross-sectioned GDEs. This confirmed that the surfaces of Cu–Zn and Cu–Pd retained terrace-dominant atomic arrangements after $\rm CO_2RR$ (Supplementary Fig. 23).

Additionally, we confirmed that the trend of adparticle formation after CO $_2$ RR remained consistent across a broad range of secondary metal contents (Supplementary Figs. 24–29). We also examined reconstruction behaviours near the interface of the Cu–X film and PTFE fibre, which serves as a triple-phase reaction interface in the GDE where gaseous CO $_2$, electrolyte and catalyst coexist 30 . Similar morphological trends were observed through SEM imaging (Supplementary Fig. 30). Furthermore, it was confirmed that the sacrificial C layer on Cu–X/PTFE does not alter the trend in catalyst reconstruction (Supplementary Figs. 31–34 and Supplementary Note 2). Finally, we demonstrated that adparticle formation from Cu–X catalysts depends on the atomic miscibility between Cu and X.

Elemental redistributions of the active materials were verified through cross-sectional TEM EDS of Cu–X catalysts before and after $\rm CO_2RR$ (Fig. 3). We confirmed that the secondary metals were relatively well dispersed in all as-synthesized Cu–X catalysts (Fig. 3a–d and Supplementary Note 3). High-resolution EDS mapping further showed that secondary metals were well distributed within the Cu lattice because of catalyst fabrication based on physical vapour deposition (Supplementary Figs. 35–41). By overcoming the thermodynamic solubility limit in

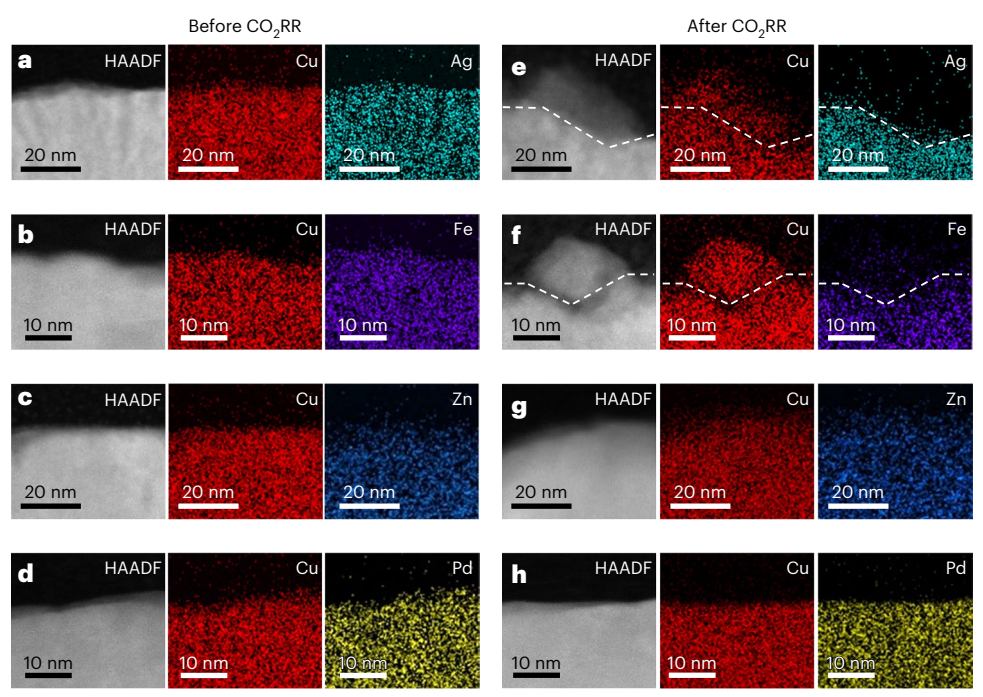


Fig. 3 | Elemental redistribution of Cu–X catalysts by CO_2RR . a–h, Cross-sectional TEM high-angle annular dark-field (HAADF) images and EDS elemental maps of the surfaces of Cu–X/PTFE GDEs (X = Ag (a and e), Fe (b and f), Zn (c and g) and Pd (d and h); -20 at.% X) before (a–d) and after (e–h) 1 h of CO₂RR at a full

cell potential of -3.6 V using 0.1 M KHCO $_3$ as the anolyte in an MEA. In ${\bf e}$ and ${\bf f}$, the white dashed lines indicate the boundaries between the adparticle and the surface grain.

catalyst fabrication, it became possible to examine the reconstruction behaviour trends based on alloying effects in both immiscible and miscible combinations, starting from nearly identical pristine states.

After CO₂RR, the Cu-Ag and Cu-Fe catalysts exhibited distinct differences in elemental distribution between the adparticles and surface grains (Fig. 3e,f). In both Cu-Ag and Cu-Fe, the adparticles displayed a Cu-rich composition, whereas the surface grains remained in a mixture state. This was further confirmed by EDS line scans in the vertical direction, where the EDS signal of secondary metals began to appear at the interface between the adparticle and the surface grain below (Supplementary Fig. 42b.d). Similar elemental segregations were also identified at other adparticles on each Cu-Ag and Cu-Fe surface (Supplementary Fig. 43). The series of high-resolution EDS spectra collected at the sub-nanometre scale in Cu-Ag clearly showed an abrupt transition in Ag distribution at the interface between the adparticle and underlying surface grain (Supplementary Fig. 44). In addition, EDS analysis for another composition of Cu-Ag (12 at.% Ag) also displayed the formation of Cu-rich adparticles on the Cu-Ag surface after CO₂RR (Supplementary Figs. 45 and 46).

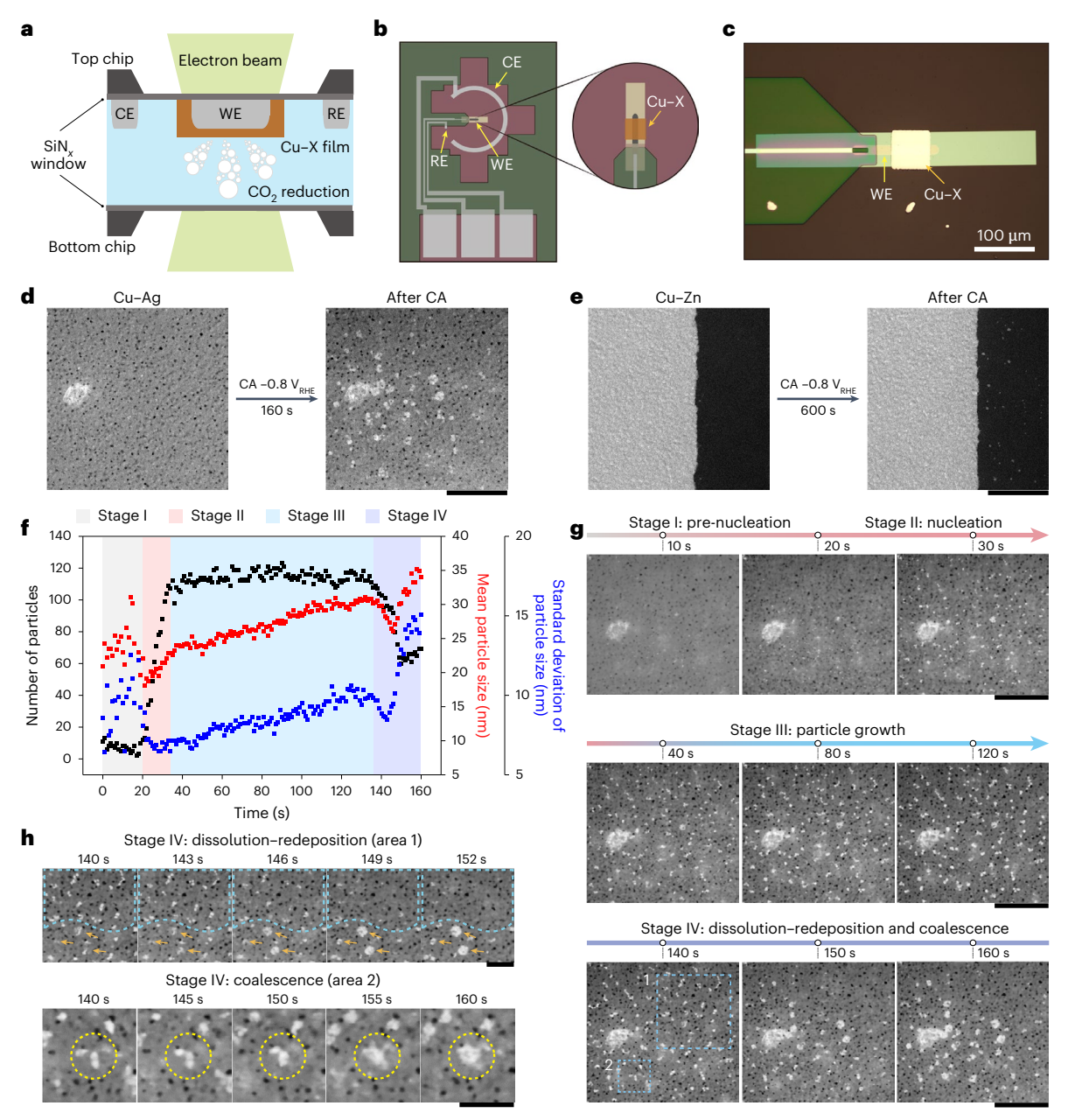
In contrast, both Cu–Zn and Cu–Pd maintained a homogeneous elemental distribution after CO $_2$ RR (Fig. 3g,h). Elemental segregation was also not observed in the EDS line profiles (Supplementary Fig. 42f,h). High-resolution EDS analysis confirmed the homogeneous distribution of Zn or Pd atoms without segregation in the Cu lattice (Supplementary Figs. 39b,d, 40b,d and 47). Moreover, a uniform elemental distribution was maintained even in the lower amounts of Zn addition, as demonstrated by TEM EDS analysis for Cu–Zn of 9 at.% Zn composition (Supplementary Figs. 48 and 49). In summary, we confirmed that the reconstructed surface states of Cu–X depend on the atomic miscibility of Cu and X, with trivial influence from their oxophilicity.

Real-time analysis of Cu-X reconstruction during CO₂RR

To investigate the dynamics of structural and chemical transformation in Cu-X catalysts during CO_2RR , in situ microscopy and spectroscopy analyses were conducted. We employed an electrochemical liquid cell

TEM (e-LCTEM) to track the structural evolution of Cu–X under an applied potential (Fig. 4a). The liquid cell comprised a top chip containing three micro-patterned electrodes and a bottom chip. The top chip included a working electrode with a 30-nm-thick Cu–Ag or Cu–Zn film (Fig. 4b,c). The assembled liquid cell was filled with CO₂-saturated 0.1 M KHCO₃ electrolyte. A potential of -0.8 V (versus the reversible hydrogen electrode (RHE)) was applied using the chronoamperometry method (Supplementary Fig. 50).

First, we confirmed that similar reconstruction trends occur by CO₂RR in liquid cells and MEAs, as demonstrated by STEM imaging, selected-area electron diffraction and EDS mapping analysis (Fig. 4d.e. Supplementary Figs. 51–53 and Supplementary Note 4). Furthermore, we demonstrated in situ formation of nanoparticles and their dynamic structural evolution, including growth, coalescence and dissolutionredeposition under cathodic potential (Supplementary Fig. 54 and Supplementary Video 1). The structural evolution of adparticles was quantitatively tracked and classified into four stages based on changes in the number and size of the particles (Fig. 4f). Stage I (pre-nucleation) was characterized by a low particle number of <10. Due to the one or two large particles, both the mean and standard deviation of the size exhibited high values. After 20 s, stage II (nucleation) occurred, whereby the Cu-Ag film became more porous, leading to the rapid formation of nuclei (Fig. 4g). The number of particles increased to >100 (Fig. 4f). This nucleation was presumably attributed to the redeposition of Cu species dissolved from the Cu-Ag film under the cathodic potential. As the number of particles became saturated, stage III (growth) began, whereby the particle sizes were steadily enlarged (Fig. 4f,g). This indicates that the Cu-Ag film was continuously dissolved after the nucleation stage. At stage IV (particle coarsening), the number of particles abruptly decreased and their sizes rapidly increased. We attribute the structural evolution to dissolution-redeposition and coalescence of the particles. Cropped in situ images of area 1, marked on Fig. 4g, show that adparticles in the blue dashed region slowly disappeared, whereas nearby particles (indicated by the orange-coloured arrows) gradually grew (Fig. 4h). This process is similar to Ostwald ripening, whereby



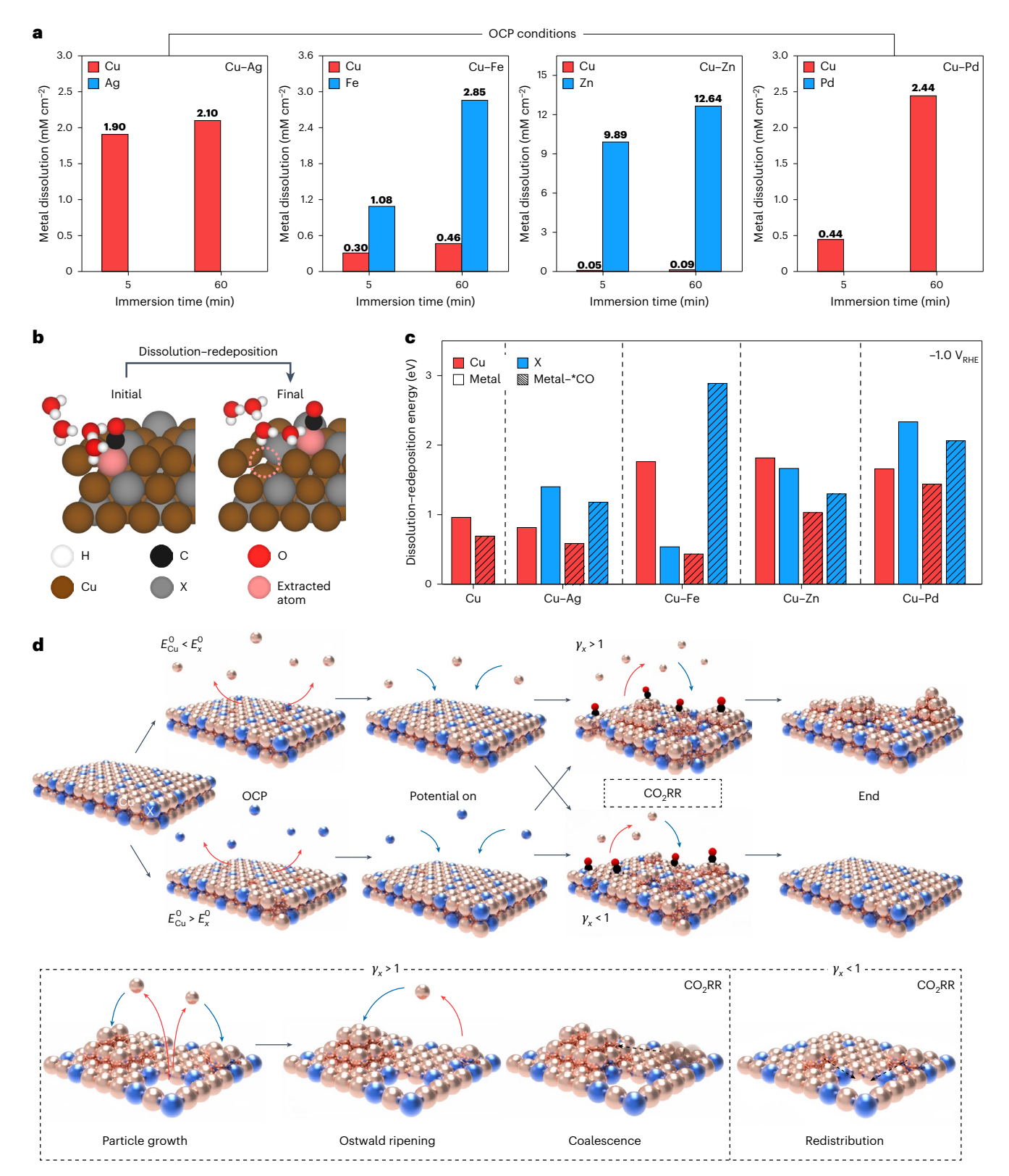
 $\label{eq:continuous} \textbf{Fig. 4} | \textbf{Real-time observation of structural evolution in Cu-X catalysts during} \\ \textbf{CO}_2\textbf{RR. a,b}, \textbf{Schematics of an e-LCTEM experimental setup (a)} \ and a top chip with a Cu-X (X = Ag or Zn) catalyst (b). c, A representative optical microscope image of a top chip with a Cu-X catalyst. d,e, STEM images of Cu-Ag (d) and Cu-Zn catalysts (e) before and after chronoamperometry (CA). Scale bars, 500 nm. f, Time-resolved structural evolution of adparticles on a Cu-Ag catalyst. The black, red and blue dots indicate the numbers, mean sizes and standard deviations of the sizes of adparticles, respectively. g, Representative STEM$

images of each stage of the structural evolution of adparticles for Cu–Ag. Scale bars, 500 nm. **h**, Cropped image series of the areas marked 1 (top) and 2 (bottom) in **g** during stage IV, presenting dissolution–redeposition and coalescence of adparticles, respectively. The blue dashed areas, orange arrows and yellow dashed circles indicate dissolution, redeposition and coalescence of adparticles, respectively. Scale bars, 200 nm. CE, counter electrode; RE, reference electrode; V_{RHE} , V versus the RHE; WE, working electrode.

dissolution of smaller particles feeds the growth of larger particles²². Cropped in situ images of area 2 exhibit coalescence of adparticles, resulting in a merged large particle (Fig. 4h).

Our in situ observations revealed that immiscible Cu–X, such as Cu–Ag, underwent surface reconstruction as the formation and growth of adparticles, based on dissolution–redeposition and coalescence mechanisms, during CO_2RR . Notably, we also found that additional morphological changes under post- CO_2RR conditions were negligible, as the structures of adparticles exhibited minimal alterations just before the end of chronoamperometry and after it (Supplementary Fig. 55 and Supplementary Note 5). Moreover, elemental redistribution

through dissolution–redeposition was tracked by comparing the EDS intensity before and after CO_2RR at an identical location in e-LCTEM (Supplementary Fig. 56). The Cu/Ag EDS ratio increased from 2.96 to 3.96 with adparticle formation by CO_2RR . Ex situ statistical analysis in e-LCTEM also exhibited an increase in the Cu/Ag ratio in adparticle regions, whereas the ratio decreased in regions without adparticles after CO_2RR (Supplementary Fig. 57). These findings suggest preferential Cu dissolution from the Cu–Ag surface, followed by redeposition, leading to the growth of Cu-rich nanoparticles. In contrast, miscible Cu–X, such as Cu–Zn, maintained its original surface structure during CO_2RR (Fig. 4e, Supplementary Fig. 58 and Supplementary Video 2).



 $\label{eq:Fig.5} \begin{tabular}{ll} Fig. 5 & | Mechanistic studies on the reconstruction of Cu-X catalysts. \\ a, Concentrations of dissolved metal ions from Cu-X/PTFE (X = Ag, Fe, Zn or Pd; -20 at.% X) into aqueous electrolyte at the OCP, quantified by ICP-MS after immersion in CO2-purged 0.1 M KHCO3. The concentration was normalized by the electrochemical surface area of each electrode.$ **b**, Schematic of a simulated dissolution–redeposition process. The extracted metal atom adsorbs near the vacancy formed on the surface. The pink dashed circle indicates the vacancy created on the surface after metal extraction.**c**, Calculated dissolution–redeposition energies of metal-on-Cu and Cu-X surfaces at -1.0 V (versus the

RHE). **d**, Schematic of the proposed reconstruction mechanism of Cu–X active materials through four sequential steps: OCP (contact with electrolyte); potential on (applying a reductive potential); CO $_2$ RR; and end (potential off). Detailed reconstruction behaviours in the CO $_2$ RR step are illustrated in the black dashed box below. The black, red, brown and blue spheres represent C, O, Cu and X, respectively. The red and blue arrows indicate dissolution and redeposition processes, respectively. γ_x and E_x^0 represent the activity coefficient of X in Cu and the standard electrode potential of X, respectively.

To track the oxidation state of Cu-X catalysts, in situ Raman spectroscopy was conducted using 1 M KHCO₂ electrolyte. This revealed that Cu oxide peaks (\sim 400, 525–534 and 615–630 cm $^{-1}$) at the open circuit potential (OCP) disappeared at -0.7 V (versus the RHE) (Supplementary Fig. 59)31. This indicates the reduction of native oxide layers to a metallic state. It was also observed that a Cu-OH peak appeared during CO₂RR and strengthened as the applied negative potential increased to -1.1 V (versus the RHE). This peak was attributed to increased local alkalinity by a high-rate CO₂RR and proton consumption, not to oxidation of the Cu lattice³². Linear combination analysis of the in situ Cu K-edge X-ray absorption near-edge structure (XANES) spectra quantitatively revealed a slight decrease in the Cu oxidation state from approximately 0.3 before CO₂RR to below 0.2 during the CO₂RR at an applied current density of 100 mA cm⁻² for all the catalysts (Supplementary Figs. 60-62). In situ Cu K-edge extended X-ray absorption fine structure analysis also showed that Cu-X catalysts maintained a metallic Cu state during CO₂RR (Supplementary Fig. 63).

However, after termination of the reductive potential, Cu oxide peaks re-appeared in the Raman spectra of Cu and Cu–Ag, whereas no peak was observed for Cu–Zn (Supplementary Fig. 59). Considering that the phases of adparticles and surface grains after CO_2RR were Cu_2O and metallic Cu, respectively, the Raman peaks corresponding to Cu_2O are attributed to the oxidized Cu adparticles (Fig. 2e,f). This confirmed that the adparticles evolved as a metallic Cu state during CO_2RR but underwent rapid oxidation upon re-exposure to OCP conditions after CO_2RR .

Mechanistic study of Cu-X reconstruction

To further clarify the underlying mechanism of reconstruction, we quantitatively examined the dissolution–redeposition behaviour of Cu–X catalysts. We proposed that this process could occur under two conditions in the CO_2RR system: (1) OCP conditions followed by the application of a reductive potential; and (2) CO_2RR conditions. Based on this approach, we investigated the dissolution–redeposition behaviour in each case.

First, to observe the dissolution behaviour under OCP conditions, dissolved metal species were detected using ICP-MS after immersing Cu–X/PTFE (-20 at.% X) in CO₂-purged 0.1 M KHCO₃ electrolyte without bias, simulating OCP conditions before initiating CO_2RR (Supplementary Fig. 64a). To account for variations in exposed surface areas, the concentration of dissolved metal ions was normalized by the electrochemical surface area of each electrode (Fig. 5a).

In Cu–X with elements less oxophilic (Ag and Pd) than Cu (E^0 = 0.34 V), substantial Cu dissolution occurred without dissolution of the secondary metals. In Cu–Ag ($E^0_{\rm Cu} < E^0_{\rm Ag}$), the concentration of dissolved Cu ions increased from 1.90 to 2.10 mM cm⁻² as the immersion time extended from 5 to 60 min, whereas Ag was not extracted. Similarly, in Cu–Pd ($E^0_{\rm Cu} < E^0_{\rm Pd}$), Cu dissolution increased from 0.44 to 2.44 mM cm⁻² over 60 min with no Pd dissolution observed over the same period. In contrast, for Cu–X with more oxophilic elements (Fe and Zn) than Cu, the secondary metals were preferentially dissolved, whereas Cu dissolution was suppressed. Specifically, Fe and Zn exhibited high dissolution levels of 2.85 and 12.64 mM cm⁻², respectively, with limited respective Cu extractions of 0.46 and 0.09 mM cm⁻² in Cu–Fe ($E^0_{\rm Cu} > E^0_{\rm Fe}$) and Cu–Zn ($E^0_{\rm Cu} > E^0_{\rm Zn}$) over 60 min of immersion. These results suggest a preferential dissolution tendency of more oxophilic elements in Cu–X under OCP conditions, similar to galvanic corrosion (Supplementary Fig. 64b)³³.

However, the amounts of dissolved metal ions were <1% of the total catalyst loading, except for 3.4% of Zn ions from the Cu–Zn electrode (Supplementary Fig. 65). This implies that even if all metal ions dissolved at the OCP were redeposited by an applied reductive potential for CO_2RR , the number of dissolved metal ions would be insufficient to form the adparticles. This was further confirmed by post-electrolysis SEM using Ar gas instead of CO_2 . After a fixed exposure time at the

OCP, no adparticle formation was observed on the Cu and Cu–X GDEs (Supplementary Fig. 66). Given the minimal extent of oxophilicity-governed dissolution under OCP conditions, we concluded that oxophilicity may not be a determining factor in reconstruction behaviour.

Instead, we focused on dissolution-redeposition behaviours under CO₂RR conditions. Our in situ TEM observations revealed that dissolution-redeposition can actively occur during CO₂RR (Fig. 4). Post-electrolysis analysis with variations in gas supply methods also confirmed that CO₂RR operation is the primary condition for dramatic surface reconstruction (Supplementary Fig. 67). To investigate elemental preferences in CO₂RR-induced dissolution-redeposition behaviour, we employed segmented electrodes with partially coated Cu-X on C/PTFE (Supplementary Fig. 68a), After 1 h of CO₂RR, redeposited nanoparticles were observed in the regions without the catalyst layer (C/PTFE). SEM EDS analysis revealed the redeposition of Cu-rich nanoparticles on C/PTFE in all cases (Supplementary Fig. 68b-f). This suggests that Cu predominantly participated in CO₂RR-driven dissolution-redeposition in Cu-X catalysts, regardless of the oxophilicity of Cu and X. Notably, a few redeposited nanoparticles were observed in the segmented electrodes of miscible combinations (Cu-Zn and Cu-Pd), whereas they were absent in the original fully coated Cu-X/PTFE electrodes used for CO₂RR. This implies that redeposited adatoms were redistributed into the miscible metallic matrix, unlike into the C matrix.

To further support this result, we evaluated the dissolution-redeposition energetics of Cu and Cu-X (X = Ag, Fe, Zn or Pd) surfaces under CO₂RR conditions using density functional theory (DFT) calculations (with an applied cathodic potential of -1.0 V (versus the RHE) on Cu (111) and Cu₃X (111) surfaces, considering a composition ratio of Cu-X (-20 at.% X)) (Fig. 5b and Supplementary Fig. 69). The dissolution-redeposition energy is referred to as E_X , where X corresponds to the metal to be dissolved and redeposited. To account for CO₂RR intermediate-induced surface reconstruction, we considered the adsorption of *CO, reported as a representative intermediate that induces the reconstruction of Cu catalysts²³. However, we found that Cu-Fe exhibits superior H₂ Faradaic efficiency (FE) during CO₂RR, whereas other catalysts mostly produced C-based products (Supplementary Fig. 70). Thus, we investigated hydrogen-covered Cu₃Fe (111) to simulate the Cu-Fe surface under CO₂RR conditions (Supplementary Fig. 71 and Supplementary Note 6). For comparison, we calculated the dissolution-redeposition energies in the absence of any adsorbates to simulate the OCP.

We found that the dissolution–redeposition energy of Cu ($E_{\rm Cu}$) decreased from 0.95 to 0.68 eV by *CO adsorption on Cu (111). This indicates that *CO could facilitate the extraction and formation of Cu adatoms during the reaction²³. Furthermore, we compared the dissolution–redeposition energies of Cu ($E_{\rm Cu}$) and X ($E_{\rm X}$) on the (111) surface of Cu₃X. In the absence of adsorbed *CO, elements with higher oxophilicity (Fe and Zn) had a higher tendency to form adatoms on each Cu₃X surface. This result aligns with the experimental observation that elements with higher oxophilicity are preferentially extracted from each Cu–X under OCP conditions, where few CO₂RR intermediates adsorb (Fig. 5a).

Interestingly, we found that the tendency for higher oxophilicity to lead to lower dissolution–redeposition energy could be tuned by the adsorption of reaction intermediates. In particular, for Cu₃Fe (111), E_{Cu} decreased from 1.76 to 0.43 eV, whereas E_{Fe} increased from 0.53 to 2.89 eV in the presence of *CO adsorbates (Fig. 5c). With adsorbates, the formation of Cu adatoms is preferred over that of Fe adatoms, despite their intrinsic oxophilicity (Fe > Cu). This theoretical result could explain the evolution of Cu adparticles from Cu–Fe by CO₂RR (Fig. 3f). Moreover, for Cu₃Ag (111), E_{Cu} decreased from 0.81 to 0.58 eV and E_{Ag} decreased from 1.40 to 1.17 eV by *CO adsorption (Fig. 5c). This result is also consistent with the evolution of Cu adparticles from Cu–Ag. For Cu₃Zn (111), E_{Cu} (1.02 eV) became lower than E_{Zn} (1.29 eV) with *CO adsorbate, despite their oxophilicity (Zn > Cu). For Cu₃Pd

(111), E_{Cu} was lower than E_{Pd} , both with and without adsorbates. We found that Cu atoms showed a greater tendency to form adatoms than secondary metals under CO_2RR conditions in all Cu–X combinations investigated. Based on consistent experimental and theoretical results, we demonstrated that the primary constituent element of adparticles is determined by the adsorbate-induced dissolution–redeposition energy, not by the intrinsic oxophilicity of the elements.

Through the various studies, involving real-time analyses, dissolution-redeposition modelling and theoretical calculations, we outlined the mechanism of Cu-X reconstruction in four sequential steps: contact with the electrolyte (the OCP); the application of a reductive potential (potential on); CO₂RR; and potential off (end) (Fig. 5d). First, in the OCP, the Cu-X surface becomes oxidized upon contact with the electrolyte and selective dissolution occurs for the element with higher oxophilicity between Cu and X. However, the numbers of dissolved metal ions are negligible compared with for the total catalyst. Second, in the step for potential on, the Cu-X surface is reduced to a metallic state and the dissolved ions are redeposited under a reductive potential. Due to negligible levels of dissolution at the OCP, the surface structure changes negligibly between the OCP step and the potential on step. Third, in the step for CO₂RR, dissolution-redeposition is facilitated by the adsorption of reaction intermediates. In Cu–Ag and Cu–Fe (y > 1), the formation of Cu adatoms is stabilized by the adsorption of reaction intermediates, regardless of their oxophilicity (Fe > Cu > Ag). Cu adatoms continuously electrodeposit with preferred Cu dissolution by CO₂RR intermediates and grow into adparticles due to atomic immiscibility. These particles then coarsen through Ostwald ripening and the coalescence mechanism. In contrast, for Cu–Zn and Cu–Pd (γ < 1), Cu adatoms are uniformly redistributed into the surface grain due to atomic miscibility. This causes the miscible bimetallic catalysts to maintain their pristine surface state. Finally, in the potential-off step, Cu adparticles are rapidly oxidized to the Cu₂O phase without morphological change in the immiscible bimetallic catalysts. For the miscible bimetallic catalysts, their metallic state of surface grains is well preserved, with a flat surface.

Effect of Cu-X reconstruction on CO₂RR selectivity

We evaluated the electrochemical CO_2RR performances of Cu and Cu-X catalysts at applied potentials ranging from -2.8 to -3.8 V in an MEA electrolyser with 0.1 M KHCO $_3$ as the anolyte. Cu generated carbon monoxide (CO) as a main CO_2RR product with a maximum FE of 63.9% at a potential of -3.0 V. As the potential increased to -3.6 V, the CO FE gradually decreased, whereas the FE of C_{2+} products increased due to enhanced *CO dimerization (Fig. 6a). At -3.6 V, C_2H_4 with an FE of 40.3% was the main product, whereas CO production was suppressed. When the potential exceeded -3.6 V, the hydrogen (H_2) FE increased to 40.0% due to promotion of the hydrogen evolution reaction, and 40.0% production was degraded with an FE of 40.0% at 40.0% calculates 40.0% due to promotion of the hydrogen evolution reaction, and 40.0% due to promotion of the hydrogen evolution reaction, and 40.0% due to promotion of the hydrogen evolution reaction, and 40.0% due to promotion of the hydrogen evolution reaction, and 40.0% due to promotion of the hydrogen evolution reaction, and 40.0% due to promotion with an FE of 40.0% at 40.0% due to promotion of the hydrogen evolution reaction, and 40.0% due to 40.0% du

The CO₂RR trends of Cu–X (~20 at.% X) were investigated by comparing the product distributions according to the applied potentials (Fig. 6b,c and Supplementary Fig. 72). Cu–Ag promoted CO production due to the presence of Ag, which can produce CO from CO₂ (Fig. 6b). At -3.2 V, Cu-Ag displayed a CO FE of 58.0%, whereas pure Cu exhibited a CO FE of 45.7%. When the potential exceeded –3.2 V, C₂H₅OH became the main CO₂RR product with an FE of 22.3%, whereas the C₂H₄ FE was suppressed to 17.5%. This suggests that Ag addition controlled the selectivity between hydrocarbon and oxygenate by steering the CO₂RR pathway from C_2H_4 to C_2H_5OH , consistent with previous reports $^{11,14,34-36}$. Furthermore, Ag addition enhanced the C₂H₅OH-to-C₂H₄ selectivity ratio from 0.55 to 1.09 at -3.6 V (Supplementary Fig. 73a). In Cu-Fe, the hydrogen evolution reaction was dominant across all applied potentials (Supplementary Fig. 72c). H₂ FEs were >50%, much higher than other Cu-X catalysts. In Cu-Zn, Zn addition suppressed *CO dimerization and favoured CO production in high-potential regions (Fig. 6c). To evaluate the degree of *CO dimerization, we calculated the ratio of C_{2+} product selectivity to that of CO and CH₄ (FE_{C2+}/FE_(CO+CH4))

(Supplementary Fig. 73b) 37 . The FE $_{C_{2+}}$ /FE $_{(CO+CH_4)}$ ratio for Cu–Zn (0.45) was considerably lower than that for Cu–Ag (5.1) at –3.6 V. Cu–Pd catalysts showed lower C $_{2+}$ FEs and higher CH $_4$ FEs compared with pure Cu (Supplementary Fig. 72e). The FE $_{C_{2+}}$ /FE $_{(CO+CH_4)}$ ratio substantially decreased from 9.1 to 1.4 at –3.6 V with Pd addition (Supplementary Fig. 73b).

We focused on the differences in CO $_2$ RR selectivity between Cu–Ag and Cu–Zn, although Ag and Zn have similar catalytic properties to induce *CO spillover near Cu 38 . We further investigated the product distributions for Cu–Ag (Ag compositions 0, 12, 18 and 28 at.%) and Cu–Zn (Zn compositions 0, 9, 17 and 28 at.%) at a fixed applied potential of –3.6 V (Fig. 6d,e). Cu–Ag maintained high C_{2+} selectivity and the FE $_{C_2H_3OH}$ /FE $_{C_2H_4}$ ratio gradually increased as the Ag content increased (Fig. 6d). For Cu–Zn, the FE $_{C_2H_3OH}$ /FE $_{C_2H_4}$ ratio rapidly increased from 1.25 to 3.54—the highest among the Cu–X catalysts—as the Zn composition was adjusted from 9 to 28 at.%. However, the CO FE for Cu–Zn abruptly increased when the Zn composition exceeded 9 at.% (Fig. 6e).

To investigate the origin of differences in catalytic performance among Cu, Cu–Ag and Cu–Zn, we conducted in situ Raman spectroscopy to investigate how *CO intermediates adsorb on the catalyst surface of Cu and Cu–X (X = Ag or Zn; -20 at.% X). The analysis was conducted in the applied potential range from -0.7 to -1.1 V (versus the RHE) in 1 M KHCO $_3$. Raman peaks for *CO bindings were observed in the regions of 250–300, 350–400, 1,950–2,000 and 2,050–2,100 cm $^{-1}$, corresponding to Cu–CO rotation, Cu–CO stretching, bridge-bound CO (CO $_{\rm bridge}$) and atop-bound CO (CO $_{\rm atop}$), respectively 39 .

To compare the *CO spillover effect in Cu-Ag and Cu-Zn with that of Cu, we investigated *CO coverage on each catalyst surface based on the Raman peaks at 200–400 cm⁻¹ (Cu–CO rotation and Cu–CO stretching)³¹. The intensity ratio of Cu-CO stretching to Cu-CO rotation is reported to be strongly correlated with *CO coverage³¹. We observed that Cu-CO peaks started to appear at lower cathodic potential in Cu-Ag compared with Cu (Fig. 6f,g). However, there was no Raman peak related to Cu-CO interaction in Cu-Zn (Supplementary Fig. 74a). At -1.1 V (versus the RHE), the intensity ratio of Cu-CO stretching to Cu-CO rotation was higher in Cu-Ag than in Cu. This indicates that the Cu-Ag surface has a higher *CO population compared with that of Cu. Furthermore, we observed a blue shift of the Cu-CO stretching peak in Cu-Ag, indicating stronger *CO binding affinity⁴⁰. Finally, we observed an additional peak at 491–494 cm⁻¹, which was assigned to Ag-CO binding in Cu-Ag^{11,41}. It can be inferred that promoted CO production at Ag sites and the stronger Cu-CO binding affinity increased *CO coverage on Cu-Ag compared with Cu. In contrast. Cu–Zn resulted in a low *CO binding affinity and facile *CO desorption.

We examined *CO binding modes (CO_{atop} and CO_{bridge}) by investigating the Raman peaks in the region of C-O stretching at 1,900-2,100 cm⁻¹ (Fig. 6h,i). For Cu and Cu–Ag, CO_{atop} and CO_{bridge} peaks simultaneously appeared and gradually strengthened as the applied potential increased from -0.7 to -1.0 V (versus the RHE) and slightly weakened at -1.1 V (versus the RHE). However, for Cu-Zn, the Raman peaks faintly appeared at -0.7 V (versus the RHE) and disappeared as the applied potential increased (Supplementary Fig. 74b). The CO_{aton}/CO_{bridge} ratio was strongly related to the *CO dimerization barrier, specifically with CO_{aton}-CO_{bridge} coupling as the most kinetically favourable, followed by CO_{atop}-CO_{atop} and CO_{bridge}-CO_{bridge}³¹. Quantification of the CO_{atop}/ CO_{bridge} ratio for Cu and Cu-Ag exhibited similar values across all measured potentials (Supplementary Fig. 75). The selectivity ratios among C₂₊ products, CH₄ and CO were also similar (Supplementary Fig. 76). These findings indicate that the preference for reaction pathways from *CO formation to dimerization, rather than hydrogenation and desorption, was comparable between Cu and Cu-Ag. In situ Raman studies revealed that efficient *CO spillover occurred on the Cu-Ag catalyst, with a moderate ratio of mixed *CO adsorption configurations. This enhanced the $FE_{C_2H_3OH}$ / $FE_{C_2H_4}$ ratio while maintaining high C_{2+} selectivity⁴². In contrast, the high CO selectivity observed in Cu–Zn was attributed to its low *CO binding affinity, which prevented further reduction of *CO intermediates.

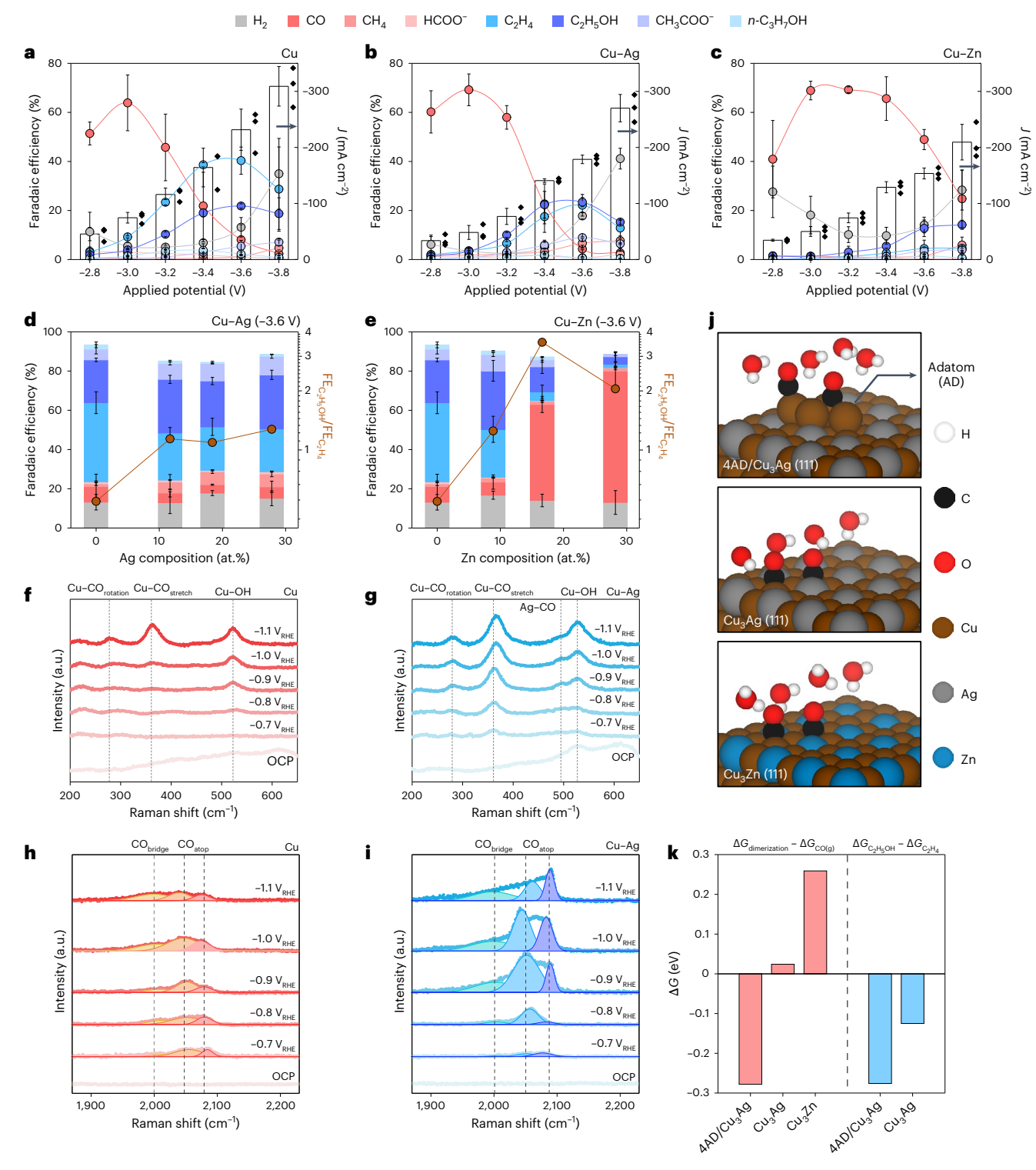


Fig. 6 | **Correlation between CO₂RR performance and the reconstruction of Cu and Cu–X catalysts.** All catalytic performances were evaluated using a C/Cu(–X)/PTFE (X = Ag and Zn) cathode in an MEA electrolyser with 0.1 M KHCO₃ as the anolyte. **a–c**, CO₂RR product distributions (coloured data points; left y axis) and current densities (f; bars; right y axis) of Cu and Cu–X (–20 at.% X) according to applied potentials from –2.8 to –3.8 V for Cu (**a**), Cu–Ag (**b**) and Cu–Zn (**c**). The data represent mean values from three independent samples and the error bars indicate standard deviation. Individual data points for f are shown in the graph, marked by diamond symbols. **d,e**, CO₂RR product distributions (coloured bars; left y axis) and C₂H₃OH-to-C₂H₄ selectivity ratios (FE_{C2H5OH}/FE_{C2H4}; brown data points; right y axis) with respect to elemental compositions of Cu–Ag (**d**) and

Cu–Zn catalysts (e). The data represent mean values from three independent samples and the error bars indicate standard deviation. **f-i**, In situ Raman spectra of Cu (**f** and **h**) and Cu–Ag (**g** and **i**) at an OCP and applied potential from –0.7 to –1.1 V (versus the RHE), displaying Cu–CO rotation and Cu–CO stretching modes (**f** and **g**) and CO $_{\text{bridge}}$ and CO $_{\text{atop}}$ modes (**h** and **i**). **j**, Side views of the atomic configurations of 2*CO adsorbed on 4AD/Cu $_3$ Ag (111), Cu $_3$ Ag (111) and Cu $_3$ Zn (111). **k**, Comparison of the reaction Gibbs free-energy differences between *CO dimerization and *CO desorption ($\Delta G_{\text{dimerization}} - \Delta G_{\text{CO(g)}}$) and bifurcation of the C $_2$ H $_3$ OH/C $_2$ H $_4$ pathway ($\Delta G_{\text{C}}_{\text{2H}_3}$ OH $-\Delta G_{\text{C}}_{\text{2H}_4}$) at –1.0 V (versus the RHE). More negative values indicate higher selectivity towards *CO dimerization and C $_2$ H $_3$ OH production, respectively.

To investigate whether *CO spillover is affected by catalyst reconstruction, we conducted a theoretical computation. We evaluated the Gibbs free energetics of reaction pathways at -1.0 V (versus the RHE) on three distinct Cu-rich sites, which are potential active sites for further reduction of diffused *CO intermediates from Ag or Zn sites: $4AD/Cu_3Ag$ (111), Cu_3Ag (111) and Cu_3Zn (111). $4AD/Cu_3Ag$ (111) was constructed to simulate Cu adparticles on the Cu-Ag surface, whereas Cu_3Ag (111) and Cu_3Zn (111) were modelled to simulate Cu-Ag and Cu-Zn surfaces, respectively (Fig. 6j).

First, we compared the reaction Gibbs free-energy differences between the *CO dimerization and *CO desorption steps at -1.0 V (versus the RHE) ($\Delta G_{\text{dimerization}} - \Delta G_{\text{CO(g)}}$). The calculations of $\Delta G_{\text{dimerization}}$ and $\Delta G_{CO(g)}$ were both referenced to the 2*CO state, defined as $\Delta G_{\text{dimerization}} = G_{\text{*OCCO}} - G_{2\text{*CO}}$ and $\Delta G_{\text{CO(g)}} = G_{\text{*CO+CO(g)}} - G_{2\text{*CO}}$. A positive value of $\Delta G_{\text{dimerization}}$ – $\Delta G_{\text{CO(g)}}$ indicates a preference for *CO desorption over *CO dimerization. Both Cu₃Ag (111) and Cu₃Zn (111) surfaces displayed positive $\Delta G_{\text{dimerization}} - \Delta G_{\text{CO(g)}}$ values, indicating favourable *CO desorption rather than dimerization. Here the energy difference was much smaller in Cu₃Ag (111) (0.02 eV) compared with Cu₃Zn (111) (0.26 eV). Therefore, *CO dimerization can occur on the Cu-Ag surface under sufficient cathodic potential. The energy difference between *CO dimerization and *CO desorption on Cu adatoms was calculated to be -0.28 eV. This negative value indicates that the presence of Cu adatoms promotes *CO dimerization on the reconstructed Cu-Ag catalyst surface. In contrast, the Cu–Zn catalyst does not form Cu adatoms via reconstruction, making dimerization less probable.

We further calculated the reaction Gibbs free-energy differences for the bifurcation between C_2H_5OH and C_2H_4 pathways $(\Delta G_{C_2H_3OH}-\Delta G_{C_2H_4})$ on $4AD/Cu_3Ag$ (111) and Cu_3Ag (111), excluding Cu_3Zn (111) due to its unfavourable conditions for *CO dimerization (Fig. 6k). The selectivity towards the C_2H_5OH and C_2H_4 pathways was determined by comparing the energetics of the reaction pathway for the formation of *CH $_3CHO$ ($\Delta G_{C_2H_5OH})$ or *O + C_2H_4 (g) ($\Delta G_{C_2H_4})$ from *CH $_2CHO$, corresponding to C_2H_5OH and C_2H_4 production, respectively 43 . 4AD/Cu $_3Ag$ (111) (-0.28 eV) exhibited a lower value of $\Delta G_{C_2H_5OH}-\Delta G_{C_2H_4}$ than Cu_3Ag (111) (-0.13 eV). This suggests that the presence of Cu adatoms further stabilizes the intermediate of the C_2H_5OH pathway on the Cu–Ag catalyst.

Our theoretical investigations revealed that the evolution of Cu adparticles in Cu–Ag provides superior active sites for promoting *CO dimerization and steering the reaction pathway towards $C_2H_5\mathrm{OH}$ production. High *CO coverage on Cu–Ag primarily originates from Cu adatoms, which efficiently suppress the desorption of *CO diffused from Ag sites. The high *CO population could make the $C_2H_5\mathrm{OH}$ pathway more favourable over the C_2H_4 pathway *2. In contrast, Cu–Zn catalyst could not provide enough active sites for efficient *CO spillover, as adparticle formation was suppressed under CO_2RR conditions. We demonstrated that the difference in reconstruction behaviours between Cu–Ag and Cu–Zn determines the C_2/C_1 selectivity ratio, as well as the $C_3H_4\mathrm{OH}/C_2H_4$ ratio.

Modulation of reconstruction dynamics and CO₂RR selectivity

We further developed a methodology to control the reconstruction of Cu–X catalysts to tune the *CO spillover effect. We speculated that surface defects could affect the reconstruction behaviour of Cu adparticle growth or stable surface retention. To explore this, Cu–Ag and Cu–Zn catalysts were subjected to pulsed potential cycles of OCP (surface oxidation) and –3.6 V (surface reduction) with a time interval of 10 s in MEAs–a process termed pulsed activation (Fig. 7a and Supplementary Fig. 77). Subsequently, CO $_2$ RR was conducted for 1 hat an applied potential of –3.6 V to investigate the effect of pulsed activation on CO $_2$ RR.

We conducted a SEM analysis of Cu–X (X = Ag or Zn; -20 at.% X) after pulsed activation and subsequent CO_2RR to investigate morphological changes (Fig. 7b). In Cu–Ag, adparticles evolved from the catalyst surface, with pore formation after 30 cycles of pulsed activation

(Fig. 7b and Supplementary Fig. 78b). After CO_2RR , the pores were diminished (Fig. 7b and Supplementary Fig. 78c). We also observed that the adparticle size after pulsed activation $(23.1 \pm 5.1 \text{ nm})$ decreased by the subsequent CO_2RR ($17.6 \pm 3.9 \text{ nm}$) (Supplementary Fig. 78e). Additionally, the size of adparticles after CO_2RR with pulsed activation ($17.6 \pm 3.9 \text{ nm}$) was much smaller than the size of particles after CO_2RR without activation ($31.3 \pm 9.4 \text{ nm}$) (Supplementary Fig. 78e). In contrast, Cu–Zn maintained a smooth surface morphology after 30 cycles of pulsed activation and subsequent CO_2RR (Fig. 7b and Supplementary Fig. 80).

We further performed a cross-sectional TEM and EDS analysis of the GDEs after CO₂RR with 30 cycles of pulsed activation. Interestingly, in Cu-Ag, Ag was distributed throughout the adparticles after CO₂RR with activation (Fig. 7c). We proceeded with EDS point mapping to quantify the Ag composition in the adparticles. In Cu-Ag after CO₂RR with pulsed activation, adparticles exhibited a mean composition of 22.1 at.% Ag-a considerably higher value compared with 1.4 at.% Ag in adparticles after CO₂RR without activation (Supplementary Fig. 82). This indicates that the surface pores facilitated Ag intermixing, and not just the diffusion of Cu adatoms into the underlying surface grain. For Cu-Zn, cross-sectional TEM analysis revealed the presence of lattice defects, such as stacking faults, in surface grains after CO₂RR with 30 cycles of pulsed activation. These were rarely observed in Cu-Zn without activation (Fig. 7d and Supplementary Fig. 83). We also confirmed a homogeneous elemental distribution after CO₂RR, regardless of pulsed activation (Supplementary Fig. 84).

We found that pulsed activation before static $\mathrm{CO_2RR}$ altered the reconstruction behaviour. Without pulsed activation, Cu adparticles were evolved from $\mathrm{Cu-Ag}$. In contrast, with pulsed activation, the growth of Cu adparticles was limited and Ag atoms became intermixed within the adparticles (Fig. 7e). Surface pores may facilitate the alloying of Cu adatoms and Ag atoms in surface grains facilitate the alloying of Cu adatoms and Ag atoms in surface grains with pulsed activation (Fig. 7f). We speculate that the structural stability under $\mathrm{CO_2RR}$ enabled $\mathrm{Cu-Zn}$ to maintain surface defects—superior active sites for * CO dimerization $\mathrm{Interior}$.

CO₂RR performance trends, according to the number of pulse cycles, were evaluated at a fixed potential of -3.6 V in MEAs. For Cu-Ag, the CO and CH₄ FEs gradually increased, whereas the C₂₊ FE was degraded as the pulse cycles increased (Fig. 7g). Specifically, the C₂H₄ FE decreased from 22.1 to 12.8% after 30 cycles of pulsed activation. whereas the C₂H₅OH FE was not notably affected by the pulse cycling. In contrast, the CO and CH₄ FEs substantially increased from 4.3 and 6.6% to 25.4 and 15.0%, respectively. Other compositions of Cu-Ag exhibited similar trends in CO₂RR selectivity changes with increasing numbers of pulse cycles (Supplementary Figs. 85 and 86). We speculate that pulsed-activation-induced Ag intermixing within the adparticles disrupts *CO dimerization and increases the number of active sites for CO and CH₄ production 46,47. In contrast, for Cu–Zn, pulsed activation promoted *CO dimerization while suppressing CO production (Fig. 7h). After ten cycles of pulsed activation, the COFE decreased from 48.9 to 30.5% and further dropped to 8.8% after 30 cycles. Under the 30-cycle condition, Cu-Zn achieved maximum C₂H₄ and C₂H₅OH FEs of 30.6 and 39.3%, respectively. It is notable that non-activated Cu-Zn was limited to C₂H₄ and C₂H₅OH FEs of 4.5 and 12.7%, respectively. The partial current densities of C₂H₄ and C₂H₅OH were also enhanced from 6.7 and 19.4 mA cm $^{-2}$ to 50.1 and 64.5 mA cm $^{-2}$, respectively, by applying 30 cycles of pulsed activation. We think that the evolution of surface $defects in \, Cu-Zn \, generated \, numerous \, active \, sites \, for \, ^*CO \, dimerization$ and enhanced *CO spillover (Supplementary Figs. 87 and 88).

We further calculated $FE_{C_{2+}}/FE_{(CO+CH_4)}$ and $FE_{C_2H_5OH}/FE_{C_2H_4}$ ratios according to the number of pulse cycles (Supplementary Fig. 89). For Cu–Ag, $FE_{C_{2+}}/FE_{(CO+CH_4)}$ decreased from 5.10 to 1.25 after 30 cycles of pulsed activation, accompanied by an increase in $FE_{C_2H_5OH}/FE_{C_2H_4}$ from 1.09 to 1.89 (Supplementary Fig. 89a,c). However, Cu–Zn displayed a

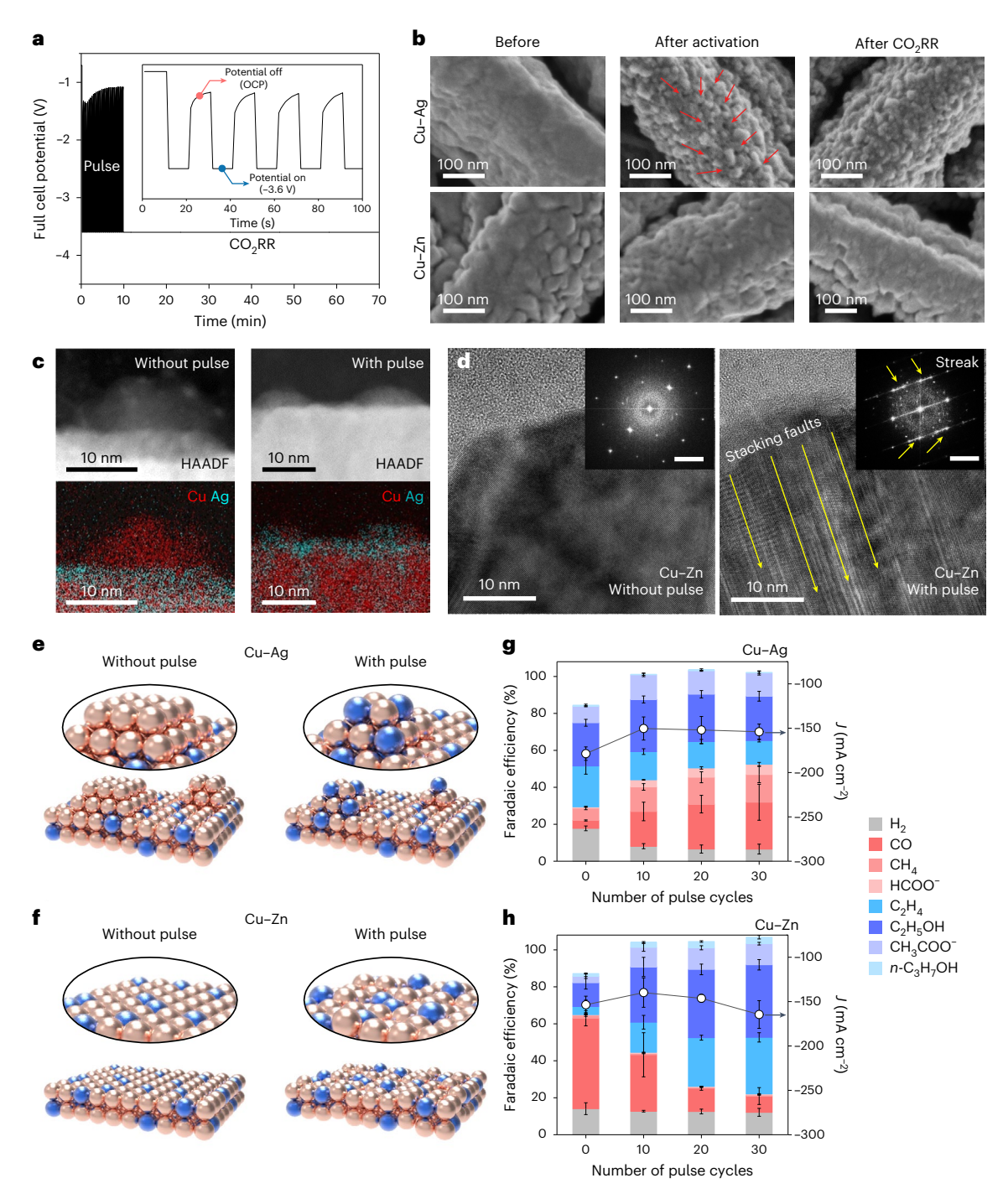


Fig. 7 | Effects of pulsed activation on Cu–X reconstruction and CO $_2$ RR selectivity. a, Representative potential profile for pulsed activation and subsequent CO $_2$ RR, where the electrode is cycled between 10 s at the OCP (surface oxidation) and 10 s at -3.6 V (surface reduction), then held at -3.6 V for 1 h. The profile represents the programme for 30 cycles of pulsed activation. b, SEM images of Cu–X (X = Ag or Zn; -20 at.% X) in the pristine state, after activation and after subsequent CO $_2$ RR. The red arrows indicate surface pores induced by pulsed activation in Cu–Ag. c, Cross-sectional TEM HAADF images (top) and EDS maps (bottom) of Cu–Ag after CO $_2$ RR, either without (left) or with

(right) 30 cycles of pulsed activation. **d**, Cross-sectional high-resolution TEM images and (inset) corresponding FFT patterns of Cu–Zn after CO₂RR, either without (left) or with (right) 30 cycles of pulsed activation. Scale bars (inset), $5\,\mathrm{nm^{-1}}$. **e**, **f**, Schematics of surface states after CO₂RR in Cu–Ag (**e**) and Cu–Zn (**f**), either without (left) or with (right) pulsed activation. The brown and blue spheres represent Cu and X, respectively. **g**, **h**, Pulse cycle-dependent CO₂RR product distributions (coloured bars; left *y* axis) and current densities (*J*; white circles; right *y* axis) for Cu–Ag (**g**) and Cu–Zn (**h**). The data represent mean values from three independent samples and the error bars indicate standard deviation.

substantial increase in FE $_{\rm C_2}$ /FE $_{\rm (CO+CH_4)}$, rising from 0.45 to 11.40 with 30 cycles of pulsed activation (Supplementary Fig. 89b,d). We have thus demonstrated controllability of reconstruction behaviours and the CO $_2$ RR pathway in Cu-based bimetallic catalysts via pulsed potential cycling before CO $_2$ RR.

Conclusions

We determined how the reconstruction of Cu bimetallic electrocatalysts proceeds during CO₂RR in MEAs. From the standard electrode potential (E^0)—activity coefficient (γ) thermodynamic elemental map, Ag ($E^0_{\text{Cu}} < E^0_{\text{Ag}}$; $\gamma_{\text{Ag}} > 1$), Fe ($E^0_{\text{Cu}} > E^0_{\text{Fe}}$; $\gamma_{\text{Fe}} > 1$), Zn ($E^0_{\text{Cu}} > E^0_{\text{Zn}}$; $\gamma_{\text{Zn}} < 1$)

and Pd ($E_{\text{Cu}}^0 < E_{\text{Pd}}^0$) $\gamma_{\text{Pd}} < 1$) were employed as X to investigate the CO2RR of Cu–X. FIB-aided cross-sectional TEM analysis of Cu–X thin films on PTFE enabled us to examine the surface states of GDEs where reconstruction occurs. Structural evolution and elemental redistribution on the catalyst surface were found to depend on the atomic miscibility of Cu and X. Immiscible elements (Ag and Fe) induced the formation of Cu-rich adparticles on the Cu–X surface, creating local elemental heterogeneity. In contrast, miscible elements (Zn and Pd) allowed for Cu–X to maintain a flat surface and homogeneous elemental distribution.

The various approaches, including real-time analyses, dissolutionredeposition model studies and DFT calculations, revealed that surface reconstruction primarily occurs through *CO-driven dissolution-redeposition during CO₂RR. *CO can change the elemental preference for dissolution away from oxophilicity-governed behaviour, resulting in selective Cu dissolution-redeposition in Cu-X. In immiscible bimetallic systems, redeposited Cu adatoms gradually grow into nanoparticles and become enlarged via Ostwald ripening and coalescence, whereas in miscible systems Cu adatoms redistribute within surface grains. Therefore, we found that atomic miscibility and *CO-modulated dissolution-redeposition energetics are key descriptors for understanding the reconstruction of bimetallic CO₂RR catalysts. Finally, we constructed an elemental map in terms of the activity coefficient and the difference between *CO-driven dissolution-redeposition energies of Cu and X, to understand the reconstruction behaviours of Cu-X (Supplementary Fig. 90). We believe that the standard electrode potential can provide information about the phase of redeposited adparticles at the working potential (as described by the Pourbaix diagram), indicating whether they exist as metals, hydroxides or oxides.

The reconstruction-induced atomic rearrangements in the active sites of Cu–X have a notable impact on the *CO spillover effect in CO $_{2}$ RR. For Cu-Ag catalysts, the dynamic evolution of Cu adatoms enabled facile *CO dimerization and promoted spillover effects to increase the selectivity ratio of C2H5OH/C2H4. However, Cu-Zn catalysts did not generate sufficient Cu adatoms (possible active sites for *CO dimerization) and primarily yielded CO through CO₂RR. Finally, the reconstruction dynamics were modulated using pulsed potential activation to control *CO spillover. In Cu-Ag, pulsed activation induced Ag intermixing within Cu adparticles, disrupting *CO dimerization and increasing CO and CH₄ production. With 30-cycle activation, the C₂H₄ FE decreased from 22.1 to 12.8% at -3.6 V, whereas the C_2H_5OH FE remained $\sim 24.0\%$. The CO and CH₄ FEs increased from 4.3 and 6.6% to 25.4 and 15.0%, respectively. In contrast, the surface stability of Cu-Zn during CO₂RR preserved potential cycling-induced surface defects, enhancing the *CO spillover effect. With 30-cycle activation, Cu-Zn achieved a maximum C₂H₅OH FE of 39.3% at -3.6 V-a 3.1-fold improvement over non-activated Cu–Zn, whereas the CO FE was suppressed to 8.8%. We believe that our findings provide a guideline for the rational design of bimetallic catalysts by predicting the evolution of desired alloy active sites during CO₂RR. This principle can be extended to understand multi-metallic catalysts such as high-entropy alloys.

Methods

Thermodynamic calculation

Activity profiles of bimetallic Cu–X were calculated using a thermochemical database program (FactSage software) based on the FTlite and SGTE databases. The activities in Cu binary systems were computed on various alloy metals at 1,800 °C, at which a liquid solution phase is stable. The activity coefficients at a 0.2-mol fraction in the binary systems were displayed in the thermodynamic elemental map (Fig. 1d and Supplementary Fig. 90).

Electrode preparation

All cathodes were prepared using a direct current magnetron sputtering system (ULTECH). Cu and Cu–X/PTFE electrodes were prepared

by sputtering 400 nm active materials on commercial PTFE membranes (Sterlitech: pore size = $0.45 \, \text{um}$) at a rate of approximately $3 \, \text{Å s}^{-1}$ under a working pressure of 4 mTorr with Ar gas (99.999%) flow. Cu-X was sputtered using the chip-on-target method. The only difference between the chip-on-target method and conventional sputtering is that small chips are placed on the main target⁴⁸. We used Ag, Fe, Zn and Pd chips (Higgs Lab; 3 mm × 3 mm × 1 mm) as small metal chips and Cu as the main target (Supplementary Fig. 11a). The alloy element and composition were controlled by the element and the number of metal chips, respectively (Supplementary Fig. 11b). Pure Cu was sputtered using a Cu target without metal chips. We cleaned the Cu targets by Ar sputtering after removing the metal chips and used a different target for each metal chip to prevent target contamination. Cu-Fe/ PTFE was prepared using Cu-Fe alloy (20 at.% Fe) target (Higgs Lab). Carbon layers were coated on as-sputtered electrodes by airbrushing a carbon black ink containing 40 mg mesoporous carbon (699632; Sigma-Aldrich; <500 nm particle size), 200 µl Nafion perfluorinated resin solution (510211; Sigma-Aldrich) and 9 ml isopropanol until the mass loading of carbon black reached 0.05 mg cm⁻². Ir oxide-coated Ti mesh (2GDL6N-025 BS20IR; Bekaert; 2 mg cm⁻² loading) was used as the anode electrode. Additionally, the segmented electrode was fabricated via a two-step sputtering process. First, 100-nm-thick amorphous C film was deposited on the PTFE membrane using a direct current sputtering system (Korea Vacuum Tech) under a working pressure of 2.5 mTorr with Argas (99.999%) flow. A graphite target (Kojundo Chemical Laboratory) was used as the sputtering target. Then, polyimide was used as a shadow mask to cover 80% of the amorphous Celectrode area, followed by sputtering of 300-nm-thick metal film under the same conditions as for the aforementioned chip-on-target sputtering.

Materials characterization

The morphology of Cu and Cu-X/PTFE GDEs was investigated by field-emission SEM (ZEISS Sigma) with an accelerating voltage of 2 kV. High-resolution TEM, high-angle annular dark-field and elemental mapping images of cross-sectioned GDEs were obtained using Cs-corrected STEM with a cold field-emission gun (JEM-ARM200F; JEOL) and an accelerating voltage of 200 kV. TEM sample preparation was performed using a dual-beam FIB SEM equipped with a micromanipulator (Crossbeam 550; ZEISS). First, protective carbon layers were deposited and then the specimen was extracted and mounted on a molybdenum grid. Thinning was conducted first at 30 kV, followed by final thinning at 2 or 5 kV. The crystal structure of the electrodes was confirmed by XRD (new D8 ADVANCE; Bruker). The XRD patterns were obtained with a scan rate of 1° s⁻¹ and a step size of 0.2°. The oxidation state and composition of the catalyst surface were analysed by XPS (Nexsa G2; Thermo Fisher Scientific). Before the analysis, the samples were slightly etched using Ar sputtering to remove the native oxide layer formed by air exposure. The XPS depth profiles were collected throughout three rounds of Ar etching, with a sputter energy of 2 kV and an interval time of 100 s. The binding energies were calibrated by referencing C 1s to 284.6 eV. The amounts of metal dissolution from the electrodes at the OCP were quantified by ICP-MS (7900 ICP-MS; Agilent). The amounts originally deposited on the electrodes were quantified by ICP-OES (5800 ICP-OES; Agilent) with acid pre-treatment.

In situ X-ray absorption spectroscopy measurements

The Cu chemical and coordination states were analysed in real-time by in situ Cu K-edge X-ray absorption spectroscopy (XAS) during $\rm CO_2RR$ at an applied current density of 100 mA cm⁻², using a flow-cell-type reactor with 1 M KHCO₃ as the electrolyte. The XAS measurements were carried out at the 10C X-ray beamline of the Pohang Accelerator Laboratory (Pohang, Republic of Korea).

In situ Raman measurements

The reaction intermediates during CO₂RR were examined by in situ Raman spectroscopy (XploRA PLUS Raman spectrometer; Horiba).

The analysis was performed using a water immersion objective lens and a 785 nm laser. The CO $_2$ flow rate was fixed at 50 sccm and 1 M KHCO $_3$ was used as the electrolyte. The Raman spectra were recorded with an acquisition time of 10 s and were collected ten times.

Electrochemical measurements

The CO₂RR performances were evaluated using an MEA electrolyser (Dioxide Materials; 5 cm² electrode area). Sustainion X37-50 (Dioxide Materials) was used as the AEM after activation in 1 M KOH followed by washing in deionized water. The electrodes and membrane were assembled together at an equal compression torque of 11 kgf cm⁻² in the MEA electrolyser. A neutral electrolyte of 0.1 M KHCO₃ (237205; Sigma-Aldrich; 99.7%) was circulated on the anode side using a peristaltic pump, whereas humidified CO₂ gas (99.999%) was supplied to the cathode side at a constant rate of 50 sccm, controlled by a mass flow controller. Full cell potentials were applied to the electrolyser using a potentiostat (ZIVE MP2). Gas chromatography (INFICON) was used to analyse the gas products, which were collected by a gas-tight syringe. Liquid products were collected from the anolyte and analysed using a high-resolution H-NMR spectrometer (600 MHz; Avance III HD; Bruker), with dimethyl sulfoxide (276855; Sigma-Aldrich) as an internal standard. All measurements were repeated three times using independent samples. In addition, liquid products of CO₂RR using D₂O-based anolyte were detected using a D-NMR spectrometer (400 MHz; Avance NEO400; Bruker).

Sample preparation for the e-LCTEM experiment

A top chip of e-LCTEM with a glassy carbon working electrode (ECT-45CR; Protochips) was prepared. The electrode-patterned side was spin-coated with a negative photoresist (ma-N 1420; micro resist technology) at 3,000 r.p.m. for 30 s, followed by baking at 100 °C for 2 min. The photoresist-coated chip was then masked around the working electrode using a photomask and exposed to ultraviolet light using an aligner (MDA-600S; MIDAS SYSTEM). By immersing the processed chip in the developer solution (ma-D 533/S; micro resist technology) for 60 s and rinsing with deionized water, the photoresist around the working electrode was removed. 30-nm-thick Cu–Ag and Cu–Zn films were sputtered using the chip-on-target method on the e-LCTEM chips. The remaining photoresist layer was removed by immersing the chip in N-methylpyrrolidone (NMP) at 55 °C for 5 min.

e-LCTEM experiments

The e-LCTEM experiments were conducted employing a commercially available liquid cell TEM holder (Poseidon Select; Protochips) and an SP-200 Potentiostat (BioLogic). STEM images were obtained using a JEM-2100F (JEOL) equipped with an UltraScan 1000XP CCD detector (Gatan) and operated at 200 kV. The Cu–X sputtered top chip, patterned with Pt counter and reference electrodes, was treated with plasma cleaning (5 mA; 90 s) under air (0.26 mbar) using an easiGlow system (PELCO) to improve its hydrophilicity. After assembling the top chip with a bottom chip, CO₂-saturated electrolyte (0.1 M KHCO₃) was flowed into the liquid cell at a flow rate of 15 μ l min $^{-1}$ until the cell was entirely filled. STEM images were acquired at a speed of 0.7 s per frame (256 \times 256 pixels with a dwell time of 10 μ s per pixel) at a beam dose of $^{-0.34}\,e^{-}$ Å $^{-2}$. Since the potential of the Pt pseudo-reference electrode is known to be 0.8 \pm 0.1 V higher than that of the RHE 25,49 , $^{-1.6}$ V versus Pt ($^{-0.8}$ V versus the RHE) was applied to the e-LCTEM setup.

In situ STEM data analysis

The contrast of in situ STEM images was enhanced using a custom-developed code from The Park Group (J.P.)⁵⁰. *K*-means clustering was then applied to remove black patches in the image, after which an FFT bandpass filter was employed in the image analysis software Fiji (ImageJ) to highlight white adparticles⁵¹. Subsequently, Otsu's thresholding was applied to binarize the adparticles. Owing to the difficulty

of thresholding in the initial 20 s of frames, the sizes of the adparticles were manually measured from the bandpass-filtered images. For statistical analysis of the adparticles, binarized particles with an area fewer than three pixels were excluded.

Ex situ characterization after e-LCTEM experiments

After carefully disassembling the liquid cell, the top chip of e-LCTEM was immersed in deionized water and gently stirred for 10 s. The chip was then immersed in acetone for 10 s and dried in air. The cleaned chip was inserted into a transmission electron microscope in an ultravacuum and then selected-area electron diffraction and EDS analysis were performed.

Computational methods

All DFT calculations were performed using the Vienna Ab initio Simulation Package (version 5.4.4) with the revised Perdew–Burke–Ernzerhof exchange–correlation functional and projector augmented wave pseudopotentials 52,53 . The D3 correction by Grimme was employed to describe the van der Waals interactions 54 . A kinetic cutoff energy of 400 eV with a Monkhorst–Pack k-point grid of (2 × 2 × 1) for Brillouin zone sampling was used for geometry optimization 55 . The convergence tolerances for energy and force during geometry optimization were set to 10^{-4} eV and 0.05 eV ${\rm \mathring{A}}^{-1}$, respectively.

We constructed the Cu and Cu–X (X = Ag, Fe, Zn or Pd) surfaces based on the optimized bulk structures of Cu and Cu₃X. The bulk structure of Cu₃X was constructed by substituting Cu atoms in the bulk FCC Cu structure with other elements, followed by full relaxation. Subsequently, we constructed a three-layered (4 × 4) (111) surface with the bottom-most layer fixed. A vacuum region of approximately 15 Å was included in the z direction. To account for the local solvent effect, four water molecules were added to the system 56 .

To simulate the electrochemical interface under a constant applied potential, we employed the grand-canonical DFT method based on the linearized Poisson–Boltzmann implicit solvation model, as implemented in VASPsol⁵⁷. In this framework, the number of electrons in the system is varied to adapt to changes in the Fermi level of the surface. The electrode potential versus the RHE of the system was identified as:

$$U_{\text{RHE}} = \frac{-(\mu_e + 4.6 \,\text{eV})}{e} + 0.0592 \times \text{pH} \tag{1}$$

where μ_e represents the Fermi level compared with the electrostatic potential of the bulk electrolyte (\textit{V}_{bulk}) and 4.6 eV represents the work function of the standard hydrogen electrode (Φ_{SHE}) predicted. The pH was set to 6.8 according to the experiments. By changing the number of electrons of the system, one can equate the μ_e of many states during electrochemical reactions, thus maintaining the potential. The calculated DFT energies were corrected to grand-canonical DFT energies as follows 39 :

$$E_{\text{GC-DFT}} = E_{\text{DFT}} - \Delta n(\mu_{\text{e}} + V_{\text{bulk}})$$
 (2)

where Δn is the number of excess electrons relative to the uncharged system.

The Gibbs free-energy corrections ($\Delta G_{\rm corr}$), including zero-point energy and enthalpic and entropic contributions, were calculated using the harmonic oscillator approximation for adsorbates and the ideal gas approximation gas molecules at 298.15 K. Thus, the Gibbs free-energy change of the reaction is given by $\Delta G = \Delta E_{\rm GC-DFT} + \Delta G_{\rm corr}$ (ref. 58).

Dissolution-redeposition energetics

To calculate the energetics of dissolution–redeposition processes, we assumed that the metal atoms are extracted from the surface and subsequently adsorb near the vacancy, forming adatoms ¹⁶. Thus, we

modelled an adatom by separating a metal atom from the surface, creating a vacancy and then placing the atom on the surface near the vacancy (Supplementary Fig. 69). Explicit water molecules were placed near the metal atom involved in the process to simulate the local solvation effect. To include the effect of adsorbates on the dissolution–redeposition energies, we added *CO to the metal atom involved in the process. Consequently, the dissolution–redeposition energies in the absence and presence of adsorbates were calculated as follows:

Without adsorbates :
$$\Delta E = E_{\text{adatom}} - E_{\text{surface}}$$
 (3)

With adsorbates :
$$\Delta E = E_{*ads+adatom} - E_{*ads+surface}$$
 (4)

where $E_{\rm adatom}$ is the energy of the slab model with an adatom and a surface vacancy, $E_{\rm surface}$ is the energy of a bare slab model, $E_{\rm *ads+adatom}$ is the energy of the slab model with an adatom and a surface vacancy with an adsorbate on the adatom, and $E_{\rm *ads+surface}$ is the energy of a bare slab model with an adsorbate.

Data availability

The optimized computational models are provided as Supplementary Data. In situe-LCTEM recordings are provided as Supplementary Videos 1 and 2. Source data are provided with this paper. All other data supporting the findings of this study are available from the corresponding authors upon reasonable request.

References

- Jordaan, S. M. & Wang, C. Electrocatalytic conversion of carbon dioxide for the Paris goals. Nat. Catal. 4, 915-920 (2021).
- Masel, R. I. et al. An industrial perspective on catalysts for low-temperature CO₂ electrolysis. Nat. Nanotechnol. 16, 118–128 (2021).
- Lee, C. W. et al. Defining a materials database for the design of copper binary alloy catalysts for electrochemical CO₂ conversion. Adv. Mater. 30, 1704717 (2018).
- Kim, C. et al. Alloy nanocatalysts for the electrochemical oxygen reduction (ORR) and the direct electrochemical carbon dioxide reduction reaction (CO₂RR). Adv. Mater. 31, 1805617 (2019).
- Ren, B. et al. Nano-crumples induced Sn-Bi bimetallic interface pattern with moderate electron bank for highly efficient CO₂ electroreduction. *Nat. Commun.* 13, 2486 (2022).
- Lee, S., Park, G. & Lee, J. Importance of Ag-Cu biphasic boundaries for selective electrochemical reduction of CO₂ to ethanol. ACS Catal. 7, 8594–8604 (2017).
- Kim, D., Resasco, J., Yu, Y., Asiri, A. M. & Yang, P. Synergistic geometric and electronic effects for electrochemical reduction of carbon dioxide using gold-copper bimetallic nanoparticles. *Nat. Commun.* 5, 4948 (2014).
- Jeon, H. S. et al. Operando insight into the correlation between the structure and composition of CuZn nanoparticles and their selectivity for the electrochemical CO₂ reduction. *J. Am. Chem.* Soc. 141, 19879–19887 (2019).
- Ren, D. et al. Atomic layer deposition of ZnO on CuO enables selective and efficient electroreduction of carbon dioxide to liquid fuels. Angew. Chem. Int. Ed. 58, 15036–15040 (2019).
- Ye, K. et al. In situ reconstruction of a hierarchical Sn-Cu/SnO_x core/shell catalyst for high-performance CO₂ electroreduction. Angew. Chem. Int. Ed. 59, 4814–4821 (2020).
- Herzog, A. et al. Operando investigation of Ag-decorated Cu₂O nanocube catalysts with enhanced CO₂ electroreduction toward liquid products. *Angew. Chem. Int. Ed.* 60, 7426–7435 (2021).
- 12. Li, L. et al. Stable, active CO_2 reduction to formate via redox-modulated stabilization of active sites. *Nat. Commun.* **12**, 5223 (2021).

- Zhu, C. et al. Dynamic restructuring of epitaxial Au–Cu biphasic interface for tandem CO₂-to-C₂₊ alcohol conversion. Chem 8, 3288–3301 (2022).
- Chen, P.-C. et al. Chemical and structural evolution of AgCu catalysts in electrochemical CO₂ reduction. *J. Am. Chem.* Soc. 145, 10116–10125 (2023).
- Okatenko, V. et al. Alloying as a strategy to boost the stability of copper nanocatalysts during the electrochemical CO₂ reduction reaction. J. Am. Chem. Soc. 145, 5370–5383 (2023).
- Li, F. et al. Interplay of electrochemical and electrical effects induces structural transformations in electrocatalysts. *Nat. Catal.* 4, 479–487 (2021).
- Kim, T. & Palmore, G. T. R. A scalable method for preparing Cu electrocatalysts that convert CO₂ into C₂, products. Nat. Commun. 11, 3622 (2020).
- Amirbeigiarab, R. et al. Atomic-scale surface restructuring of copper electrodes under CO₂ electroreduction conditions. Nat. Catal. 6, 837–846 (2023).
- Lee, S. H. et al. Oxidation state and surface reconstruction of Cu under CO₂ reduction conditions from in situ X-ray characterization. J. Am. Chem. Soc. 143, 588–592 (2021).
- 20. Wang, J., Tan, H.-Y., Zhu, Y., Chu, H. & Chen, H. M. Linking the dynamic chemical state of catalysts with the product profile of electrocatalytic CO_2 reduction. *Angew. Chem. Int. Ed.* **60**, 17254–17267 (2021).
- Grosse, P. et al. Dynamic transformation of cubic copper catalysts during CO₂ electroreduction and its impact on catalytic selectivity. Nat. Commun. 12, 6736 (2021).
- Vavra, J., Shen, T.-H., Stoian, D., Tileli, V. & Buonsanti, R. Real-time monitoring reveals dissolution/redeposition mechanism in copper nanocatalysts during the initial stages of the CO₂ reduction reaction. *Angew. Chem. Int. Ed.* 60, 1347–1354 (2021).
- Vavra, J. et al. Solution-based Cu⁺ transient species mediate the reconstruction of copper electrocatalysts for CO₂ reduction. Nat. Catal. 7, 89–97 (2024).
- Huang, J. et al. Potential-induced nanoclustering of metallic catalysts during electrochemical CO₂ reduction. *Nat. Commun.* 9, 3117 (2018).
- Yang, Y. et al. Operando studies reveal active Cu nanograins for CO₂ electroreduction. *Nature* 614, 262–269 (2023).
- 26. Nam, D.-H. et al. High-rate and selective CO_2 electrolysis to ethylene via metal–organic-framework-augmented CO_2 availability. *Adv. Mater.* **34**, 2207088 (2022).
- Choi, W. et al. Origin of hydrogen incorporated into ethylene during electrochemical CO₂ reduction in membrane electrode assembly. ACS Energy Lett. 7, 939–945 (2022).
- 28. Kim, J.-Y. et al. Selective hydrocarbon or oxygenate production in CO_2 electroreduction over metallurgical alloy catalysts. *Nat. Synth.* **3**, 452–465 (2024).
- 29. Leitner, J., Sedmidubský, D., Lojka, M. & Jankovský, O. The effect of nanosizing on the oxidation of partially oxidized copper nanoparticles. *Materials (Basel)* **13**, 2878 (2020).
- García de Arquer, F. P. et al. CO₂ electrolysis to multicarbon products at activities greater than 1A cm⁻². Science 367, 661–666 (2020).
- 31. Zhan, C. et al. Revealing the CO coverage-driven C–C coupling mechanism for electrochemical CO_2 reduction on Cu_2O nanocubes via operando Raman spectroscopy. ACS Catal. 11, 7694–7701 (2021).
- An, H. et al. Sub-second time-resolved surface-enhanced Raman spectroscopy reveals dynamic CO intermediates during electrochemical CO₂ reduction on copper. *Angew. Chem. Int. Ed.* 60, 16576–16584 (2021).

- 33. McCafferty, E. Introduction to Corrosion Science (Springer, 2010).
- 34. Li, Y. C. et al. Binding site diversity promotes CO₂ electroreduction to ethanol. *J. Am. Chem.* Soc. **141**, 8584–8591 (2019).
- Iyengar, P., Kolb, M. J., Pankhurst, J. R., Calle-Vallejo, F. & Buonsanti, R. Elucidating the facet-dependent selectivity for CO₂ electroreduction to ethanol of Cu–Ag tandem catalysts. ACS Catal. 11, 4456–4463 (2021).
- Chen, C. et al. Exploration of the bio-analogous asymmetric C-C coupling mechanism in tandem CO₂ electroreduction. Nat. Catal. 5, 878–887 (2022).
- Shin, S.-J. et al. A unifying mechanism for cation effect modulating C₁ and C₂ productions from CO₂ electroreduction. Nat. Commun. 13, 5482 (2022).
- Bagger, A., Ju, W., Varela, A. S., Strasser, P. & Rossmeisl, J. Electrochemical CO₂ reduction: a classification problem. ChemPhysChem 18, 3266–3273 (2017).
- Kim, J. et al. Vitamin C-induced CO₂ capture enables high-rate ethylene production in CO₂ electroreduction. Nat. Commun. 15, 192 (2024).
- 40. Wang, X. et al. Efficient electrically powered CO_2 -to-ethanol via suppression of deoxygenation. *Nat. Energy* **5**, 478–486 (2020).
- Gao, J. et al. Selective C–C coupling in carbon dioxide electroreduction via efficient spillover of intermediates as supported by operando Raman spectroscopy. J. Am. Chem. Soc. 141, 18704–18714 (2019).
- Li, F. et al. Cooperative CO₂-to-ethanol conversion via enriched intermediates at molecule–metal catalyst interfaces. *Nat. Catal.* 3, 75–82 (2020).
- Wang, D. et al. Revealing the structural evolution of CuAg composites during electrochemical carbon monoxide reduction. Nat. Commun. 15, 4692 (2024).
- Sprunger, P. T., Lægsgaard, E. & Besenbacher, F. Growth of Ag on Cu(100) studied by STM: from surface alloying to Ag superstructures. *Phys. Rev. B* 54, 8163–8171 (1996).
- 45. Gu, Z. et al. Efficient electrocatalytic CO_2 reduction to C_{2+} alcohols at defect-site-rich Cu surface. *Joule* **5**, 429–440 (2021).
- Chang, C.-J. et al. Dynamic reoxidation/reduction-driven atomic interdiffusion for highly selective CO₂ reduction toward methane.
 J. Am. Chem. Soc. 142, 12119–12132 (2020).
- Wei, D. et al. Decrypting the controlled product selectivity over Ag–Cu bimetallic surface alloys for electrochemical CO₂ reduction. Angew. Chem. Int. Ed. 62, e202217369 (2023).
- 48. Kim, C. et al. Robust Co alloy design for Co interconnects using a self-forming barrier layer. Sci. Rep. **12**, 12291 (2022).
- Yang, Y. et al. Elucidating cathodic corrosion mechanisms with operando electrochemical transmission electron microscopy. J. Am. Chem. Soc. 144, 15698–15708 (2022).
- Kim, J. et al. Self-supervised machine learning framework for high-throughput electron microscopy. Sci. Adv. 11, eads5552 (2025).
- Schindelin, J. et al. Fiji: an open-source platform for biological-image analysis. *Nat. Methods* 9, 676–682 (2012).
- 52. Kresse, G. & Furthmüller, J. Efficiency of ab-initio total energy calculations for metals and semiconductors using a plane-wave basis set. *Comput. Mater. Sci.* **6**, 15–50 (1996).
- Hammer, B., Hansen, L. B. & Nørskov, J. K. Improved adsorption energetics within density-functional theory using revised Perdew– Burke–Ernzerhof functionals. *Phys. Rev. B* 59, 7413–7421 (1999).
- 54. Grimme, S., Ehrlich, S. & Goerigk, L. Effect of the damping function in dispersion corrected density functional theory. *J. Comput. Chem.* **32**, 1456–1465 (2011).

- Monkhorst, H. J. & Pack, J. D. Special points for Brillouin-zone integrations. Phys. Rev. B 13. 5188–5192 (1976).
- 56. Hao, Y.-C. et al. Promoting nitrogen electroreduction to ammonia with bismuth nanocrystals and potassium cations in water.

 Nat. Catal. 2. 448–456 (2019).
- 57. Mathew, K., Kolluru, V. S. C., Mula, S., Steinmann, S. N. & Hennig, R. G. Implicit self-consistent electrolyte model in plane-wave density-functional theory. *J. Chem. Phys.* **151**, 234101 (2019).
- Hjorth Larsen, A. et al. The atomic simulation environment—a Python library for working with atoms. *J. Phys. Condens. Matter* 29, 273002 (2017).

Acknowledgements

This research was supported by National Research Foundation of Korea (NRF) grants funded by the Korean government's Ministry of Science and ICT (MSIT) (RS-2021-NR061733 and NRF-2021M3D1A2047041 to D.-H.N.). Y.-C.J. acknowledges support from the Creative Materials Discovery Program through the NRF, funded by MSIT and Future Planning (2017M3D1A1040689), as well as from an NRF grant funded by the Korean government's MSIT (RS-2024-00457199). J.P. acknowledges support from the NRF, funded by MSIT (RS-2024-00421181 and RS-2024-00449965). S.B. acknowledges the support from the Nano and Material Technology Development Program through the NRF funded by MSIT (RS-2024-00406517) and generous supercomputing time from Korea Institute of Science and Technology Information. We acknowledge support received from the Hanwha Solutions Chemical Division. We thank B. Jeon, G. Kim and K. Seob Song of the Catalysis Technology Center of the Hanwha Solutions Chemical Division for valuable support. Material characterization, including grazing incidence XRD, SEM and TEM analyses, was supported by the Research Institute of Advanced Materials and National Center for Inter-University Research Facilities at Seoul National University. ICP-MS, NMR analysis and FIB preparation were supported by the National Instrumentation Center for Environmental Management at Seoul National University. XPS analysis was supported by the Korea Institute of Ceramic Engineering and Technology. Experiments at Pohang Light Source II were supported in part by MSIT and Pohang University of Science and Technology.

Author contributions

D.-H.N., Y.-C.J., J.P. and S.B. designed and supervised the overall project. I.K., G.-B.L., S.K. and H.D.J. conceived of the idea and conducted the experiments. I.K. and G.-B.L. carried out electrode fabrication, characterization and electrochemical measurements. S.K. performed the e-LCTEM experiments with assistance from H.C. under the supervision of J.P. H.D.J. conducted the DFT calculations and analyses under the supervision of S.B. J.-Y.K. contributed to CO₂RR performance evaluation. T.L. carried out the real-time XAS and Raman analyses with the assistance of Y.L. J.J. performed the high-resolution TEM EDS. H.G.K. contributed to TEM measurement under the supervision of M.K. G.K. contributed to thermodynamic calculations. S.-H.O. contributed to SEM measurement and analysis. W.K. contributed to XPS analysis. D.H. and J.-Y.K. contributed to data analysis. U.K. contributed to fabrication. H.K. contributed to SEM EDS analysis of the segmented electrodes. All authors discussed the results and contributed to writing the paper.

Competing interests

The authors declare no competing interests.

Additional information

Supplementary information The online version contains supplementary material available at https://doi.org/10.1038/s41929-025-01368-9.

Correspondence and requests for materials should be addressed to Seoin Back, Jungwon Park, Young-Chang Joo or Dae-Hyun Nam.

Peer review information *Nature Catalysis* thanks the anonymous reviewers for their contribution to the peer review of this work.

Reprints and permissions information is available at www.nature.com/reprints.

Publisher's note Springer Nature remains neutral with regard to jurisdictional claims in published maps and institutional affiliations.

Springer Nature or its licensor (e.g. a society or other partner) holds exclusive rights to this article under a publishing agreement with the author(s) or other rightsholder(s); author self-archiving of the accepted manuscript version of this article is solely governed by the terms of such publishing agreement and applicable law.

© The Author(s), under exclusive licence to Springer Nature Limited 2025

Department of Materials Science and Engineering, Seoul National University, Seoul, Republic of Korea. Department of Chemical and Biological Engineering, Institute of Chemical Processes, Seoul National University, Seoul, Republic of Korea. Chemical Processes, Seoul National University, Seoul, Republic of Korea. Department of Chemical and Biomolecular Engineering, Institute of Emergent Materials, Sogang University, Seoul, Republic of Korea. Department of Energy Science and Engineering, Daegu Gyeongbuk Institute of Science and Technology, Daegu, Republic of Korea. Department of Materials Science and Engineering, Korea University, Seoul, Republic of Korea. Korea University, Seoul, Republic of Korea. Department of Integrative Energy Engineering, Korea University, Seoul, Republic of Korea. Institute of Engineering Research, College of Engineering, Seoul National University, Seoul, Republic of Korea. Seoul National University, Seoul, Republic of Korea. Department of Chemistry and Chemical Biology, Cornell University, Ithaca, NY, USA. These authors contributed equally: Intae Kim, Gi-Baek Lee, Sungin Kim, Hyun Dong Jung. Pe-mail: Sback@korea.ac.kr; jungwonpark@snu.ac.kr; cham@korea.ac.kr